# Tropical 40–50- and 25–30-Day Oscillations Appearing in Realistic and Idealized GFDL Climate Models and the ECMWF Dataset

Y. HAYASHI AND D. G. GOLDER

*Geophysical Fluid Dynamics Laboratory/NOAA, Princeton University, Princeton, New Jersey*

(Manuscript received 28 May 1991, in final form 27 April 1992)

## ABSTRACT

To clarify differences between the tropical 40–50- and 25–30-day oscillations and to evaluate simulations and various theories, space–time spectrum and filter analyses were performed on a nine-year dataset taken from the nine-level R30 spectral general circulation model and the nine-year (1979–1987) ECMWF four-dimensional analysis dataset. In addition, the 40-level SKYHI model was analyzed to examine the effect of increased vertical resolution, while an ocean-surface perpetual January R30 model was analyzed to examine the effects of the absence of geographical and seasonal variations.

The R30 model results indicate that the relative amplitude of the wavenumber-one component of the 40–50- and 25–30-day oscillations varies greatly from year to year. For the nine-year average, the simulated 40–50-day zonal velocity oscillations are as strong as observed, while the simulated 25–30-day zonal velocity oscillations are much stronger than observed. Although 40–50- and 25–30-day oscillations have similar structures, the 25–30-day oscillations exhibit a greater increase with height in their tropospheric amplitudes than the 40–50-day oscillations, resulting in different relative magnitudes at different levels. The time variance of the two oscillations has similar longitudinal distributions, implying that the two periods are not due to differences in local phase speeds. They appear to grow and decay independently without any coherent phase relationship, implying that the two periods are not a result of the seasonal modulation of an intrinsic 30–40-day period.

The SKYHI model indicates that 25–30-day oscillations still appear too strong. Nevertheless, this model reveals a longer vertical wavelength, a higher penetration of the 25–30-day amplitude above the level of convective heating, and a slightly greater height of the convective-heating amplitude, which cannot be detected in the R30 model. This implies that the two oscillations differ in their intrinsic vertical wavelengths.

The ocean-surface perpetual January R30 model indicates that not only the 25–30-day mode but also the 40–50-day mode can be simulated in the absence of geographical and seasonal modulations, while the wave-CISK and evaporation–wind feedback theories cannot explain the 40–50-day mode. Both R30 models indicate that daily precipitation is almost always associated with upward motion, being consistent with theoretical conditional heating. A comparison between the two R30 models suggests that the sea surface temperature geographically modulates the intrinsically eastward-moving wavenumber-one precipitation oscillations, resulting in their major Pacific and minor Atlantic local amplitudes. This in turn causes planetary-scale eastward-moving zonal-velocity oscillations and standing geopotential oscillations.

## 1. Introduction

Since their discovery by Madden and Julian (1971), there have been numerous observational, numerical, and theoretical studies of tropical intraseasonal oscillations. A brief review of these studies can be found in several papers (e.g., see Hayashi and Golder 1986; Park et al. 1990; Magana and Yanai 1991).

In Hayashi and Golder (1986, 1988), space–time spectrum and filter analyses were conducted to study the propagation and structure of the tropical intraseasonal oscillations appearing in GFDL spectral general circulation models and those found in the GFDL FGGE four-dimensional assimilation dataset. The models had rhomboidal truncation at wavenumbers 30 and 15 (hereafter referred to as R30 and R15).

The results indicated that the R30 model exhibited wavenumber-one spectral peaks in the equatorial zonal velocity at eastward-moving periods of 40–50 and 25–30 days. The 40–50-day peak was, however, not as pronounced as that found in the FGGE data, while the 25–30-day peak was as strong as that found in the FGGE data. On the other hand, the R15 model exhibited a broad 20–40-day peak but failed to reproduce a distinct 40–50-day peak, being consistent with the time-spectral analysis of the same GFDL R15 model by Lau and Lau (1986) and the NCAR R15 model by Pitcher and Geisler (1987).

The defects in the relative amplitudes of the 40–50- and 25–30-day oscillations will cause simulated intraseasonal oscillations to propagate too fast, resulting in the degradation of tropical weather predictions made

---

*Corresponding author address:* Dr. Yoshikazu Hayashi, Geophysical Fluid Dynamics Laboratory, Princeton University, P.O. Box 308, Princeton, NJ 08542.

with the R30 model. Nevertheless, the R30 model results demonstrate that both the 40–50- and 25–30-day oscillations can be qualitatively well simulated in a realistic general circulation model, even in the absence of air–sea interactions and cloud–radiation feedbacks.

These 40–50- and 25–30-day oscillations exhibited similar structures in spite of the difference in their time scales. In particular, both oscillations were characterized by a phase reversal between the upper- and lower-tropospheric zonal velocities. This is consistent with the oscillation and zonal propagation of the Walker (zonal–vertical) cell, as observationally suggested by Madden and Julian (1972).

Both oscillations were found to exhibit the form of a Kelvin–Rossby wave pattern in the upper troposphere and a Rossby wavelike pattern in the lower troposphere. Further, they displayed the form of a latitudinally tilted Walker cell, modified by meridional convergence in the boundary layer and characterized by the westward tilt of vertical velocity with height in the lower troposphere. The latitudinal tilt is consistent with the northward propagation of observed intraseasonal oscillations found by Yasunari (1981). The westward tilt of vertical velocity is due to boundary-layer convergence, involving both the zonal and meridional velocities.

Since these simulated and observed results were based on data for a particular year, however, it was inconclusive as to whether or not the long-term average amplitude of the simulated 40–50-day oscillations was weaker than that observed. In particular, the FGGE year may not be a representative year for the study of the general circulation and eddy statistics, as cautioned by Trenberth (1984) on the basis of a long-term Southern Hemisphere dataset. Moreover, since theoretical wavenumber-one Kelvin waves with different periods do not have exactly the same structure, the 40–50- and 25–30-day oscillations may be associated with subtle structural differences that cannot be detected over a short-term record.

There is also the possibility that the simulated oscillations may exhibit different vertical structures and more realistic amplitudes when the vertical resolution is increased. The 40–50- and 25–30-day periods might be a result of differing local phase speeds that depend on local basic flows or a result of a seasonal modulation of an intrinsic 30–40-day period. If this is the case, intraseasonal oscillations could be associated with a single 30–40-day peak in the absence of seasonal and geographical variations, being consistent with intraseasonal wave-CISK theory (Miyahara 1987; Lau and Peng 1987) and evaporation–wind feedback theory (Neelin et al. 1987; Emanuel 1987) as well as ocean-surface general circulation experiments (Hayashi and Sumi 1986; Neelin et al. 1987). The 40–50-day oscillations might also result from interactions with the ground hydrology, as suggested by the dynamical models of Webster and Chou (1980) and Webster (1983).

The purposes of the present paper are to clarify the differences between 40–50- and 25–30-day oscillations and to evaluate simulations and various theories in comparison with observed data. To accomplish these, space–time spectrum and filter analyses are performed on nine years of data from the nine-level R30 model and the nine-year (1979–1987) ECMWF four-dimensional analysis dataset, which includes the FGGE year of 1979. The effects of higher vertical resolution are examined through the use of the 40-level SKYHI model, while the influences of removing geographical and seasonal variations are studied with an R30 ocean-surface perpetual January model. The tropical–extratropical interactions of intraseasonal oscillations are beyond the scope of the present paper.

Section 2 reviews several theories pertaining to intraseasonal oscillations, while section 3 describes the model and observed data used. Sections 4 and 5 examine the spectral distribution and structure of the oscillations, respectively, improving the previous results of Hayashi and Golder (1986, 1988) by making use of long-term data. Section 6 presents the results of the SKYHI model, while section 7 examines the ocean-surface model. Conclusions and remarks are given in section 8.

## 2. A review of theories of intraseasonal oscillations

In this section, several theories relevant to the present study are reviewed to provide a theoretical background for the examination of intraseasonal oscillations. Implications of the present study with respect to these theories will be given in section 8.

### a. *Viscous gravity-wave theory*

Observed low-frequency intraseasonal oscillations have posed a number of interesting theoretical problems. Chang (1977) pointed out that the intrinsic vertical wavelength of a wavenumber-one 40–50-day period Kelvin wave is only 8–9 km. This wavelength was determined through the dispersion relation in the presence of a basic easterly zonal wind of 5 m $s^{-1}$. The determined value is too short to explain the observed vertical wavelength of 15–30 km and is also highly sensitive to the period and the basic flow. To explain this discrepancy, Chang proposed that the intrinsic vertical wavelength can be modified to the observed value by taking into account the effect of strong viscosity due to cumulus momentum transport.

When the waves are thermally forced or the vertical distribution of the parameterized convective heating is prescribed, however, the resulting vertical scale in the heating layer is determined by the vertical scale of the heating rather than the intrinsic vertical wavelength. If condensational heating is proportional to the vertical velocity, the static stability is effectively reduced, resulting in a longer vertical wavelength. The intrinsic vertical wavelength manifests itself only above the heating layer.

### *b. Thermal-forcing theory*

To study the propagation and structure of intraseasonal oscillations Yamagata and Hayashi (1984) modified the two-dimensional model (Gill 1980) of thermally forced tropical stationary waves. The modified model accommodated transient waves by prescribing a localized thermal forcing that oscillates with a 40-day period. It was found that the resulting intraseasonal oscillations were characterized by a combined Kelvin–Rossby wave pattern of Matsuno (1966) and Gill (1980), the Kelvin and Rossby modes propagating to the east and west of the localized forcing, respectively. Subsequently, this pattern was identified in both the FGGE data and the R30 model by Hayashi and Golder (1986). The pattern was found to propagate eastward, however, contrary to the westward propagation of the Rossby-mode pattern.

To improve Yamagata and Hayashi's results, Hayashi and Miyahara (1987) assumed that the amplitude of eastward-moving wavenumber-one heating is geographically modulated. The localized amplitude results in a high local wavenumber and therefore a slow local phase speed, even in the absence of a local easterly basic flow. They also found that when small-amplitude eastward-moving heating was allowed outside the area of the localized heat source, the Kelvin–Rossby wave pattern propagated eastward, their zonal velocity amplitude being stronger in the region of weaker heating than in the region of stronger heating, in agreement with the FGGE data (Maruyama 1982; Hayashi and Golder 1986). When the eastward-moving heating was strictly localized, the Rossby mode propagated westward, as in the case of a localized heat pulsation. Their model differs from the thermal-forcing model of Chao (1987) in which the localized heat source is not geographically fixed but moves eastward.

Itoh and Nishi (1990) reexamined the case of strictly confined eastward-moving thermal forcing and showed that the westward-propagating Rossby mode can be suppressed, depending on the damping time and the local phase speed of the forcing. Thus, on the basis of thermal-forcing models, it is inconclusive as to whether the global eastward propagation of zonal velocity results from global or local eastward propagation of the heating. Moreover, these thermal-forcing models, by their nature, do not explain how the period and scale of the observed heating are determined.

### *c. Random thermal-forcing theory*

To explain the selection of stratospheric 10–20-day Kelvin waves (Wallace and Kousky 1968) and 4–5-day mixed Rossby–gravity waves (Yanai and Maruyama 1966) in the stratosphere, Holton (1973), Hayashi (1976), and Chang (1976) examined the linear response of equatorial waves to white-noise thermal forcing having a coherent structure. They found that a maximum response occurs for a given wavenumber and frequency close to those observed when the intrinsic vertical scale matches the vertical scale of the forcing.

This response has a finite amplitude and differs from the infinite-amplitude resonance of free oscillations. The free oscillations of a hypothetical finite-depth atmosphere have discrete vertical wavenumbers that depend on the depth, while those of an infinite-depth atmosphere have continuous wavenumbers. The sharp peak found in the frequency response is due to the period of the Kelvin and mixed Rossby–gravity waves being rather insensitive to the intrinsic vertical scale.

In spite of the plausible explanation of the observed wave selectivity, Hayashi (1976) found that the vertical velocity and heating of the maximum-response waves were not balanced in amplitude, being nearly 90° out of phase and contrary to the results from a GFDL general circulation model. This defect is due to the absence of the feedback from the forced waves to the forcing. Moreover, convective heating related to planetary-scale waves probably has a coherent structure and spectral peaks, while convective heating unrelated to planetary-scale waves probably has an incoherent structure and no spectral peaks. It is inappropriate to impose random thermal forcing having a coherent structure.

A red-noise heating can result from sporadic and localized heating that has a coherent structure. Salby and Garcia (1987) and Garcia and Salby (1987) reproduced the 10–20- and 40–50-day Kelvin modes by use of a linear response model having an intermittent red-noise thermal forcing. This assumption is, however, contrary to the observed outgoing longwave radiation (Nakazawa 1986) and simulated precipitation (Hayashi and Golder 1986); both of which are associated with spectral peaks at intraseasonal periods.

The response of waves to tropospheric thermal forcing is also due to the vertical propagation of energy. Since Kelvin waves having slow phase speeds are associated with a slow vertical group velocity, intraseasonal oscillations are confined to the troposphere, while 10–20-day Kelvin waves can penetrate into the stratosphere.

### *d. Wave–CISK theory*

Recently, there has been a renewed interest in the wave–CISK theory to explain the preferred scale and structure of intraseasonal oscillations. This theory was first proposed by Hayashi (1970) and reexamined by Lindzen (1974) to explain the stratospheric 4–5-day mixed Rossby–gravity waves and 10–15-day Kelvin waves. This theory assumes that the ensemble effect of cumulus heating is proportional to the wave convergence of moisture in the surface layer. If the waves generated by the large-scale heating produce convergence in the region of heating, this feedback can result in unstable oscillatory waves. In contrast, when the dry static stability is simply replaced by moist static stability, unstable waves become stationary.

It was found (Hayashi 1970) that both the Kelvin and mixed Rossby–gravity waves become unstable, with their structures strikingly similar to those observed. In spite of these favorable results, their growth rates increased with frequency and the shortest-scale Kelvin and gravity waves became the most unstable, contrary to those observed.

It was further shown that the growth rates were significantly enhanced by frictional convergence (Hayashi 1971b), while they were somewhat reduced by an energy loss to the upper atmosphere under the radiation boundary condition (Hayashi 1971c). Nevertheless, the growth rates still increased with frequency. Recently, Wang (1988) analytically reexamined low-frequency Kelvin wave–CISK in the presence of surface friction, finding that a preferred scale occurred at low wavenumbers for strong Newtonian cooling. Xie and Kubokawa (1990) pointed out, however, that Wang's finding resulted from neglecting the meridional velocity in the free atmosphere, thus numerically confirming the original conclusion of Hayashi (1971b) that the growth rate increases with frequency.

In an effort to alleviate these defects, Hayashi (1971d) and Kuo (1975) assumed that the heating parameter was dependent on wave frequency. The physical interpretation of this modification is that convection will depend on the oscillation of moisture itself rather than moisture convergence, resulting in a phase lag between the heating and convergence (Davis 1979). Although this modification resulted in the observed preferred scale and a suppression of high-frequency gravity waves, the physical assumption must be justified.

To explain the observed intraseasonal periodicity and wavenumber structure, wave–CISK theory has recently been modified by imposing conditional heating that permits only positive heating due to condensation (Lau and Peng 1987; Miyahara 1987; Yamagata 1987; Hendon 1988; Itoh 1989; Davey 1989; Lim et al. 1990; Dunkerton and Crum 1991; Yoshizaki 1991; Crum and Dunkerton 1992). When this condition is applied to a region of an ensemble of convective heating, it can be interpreted as convection seldom occurring in the area of a large-scale divergence field.

It was found that 25–30-day Kelvin waves dominantly appear in these numerical models. This period is longer than the 15-day period found in the original wave–CISK theory. This difference is due to the vertical distribution of convective heating, which was assumed to be strongest in the upper troposphere in the original theory and in the middle troposphere of the modified models, as clarified by Takahashi (1987) and Chang and Lim (1988). Although the phase speed of the wave–CISK modes depends on the effective moist static stability, it should not be interpreted as the moist-reduced phase speed of free oscillations. The latter phase speeds depend on the arbitrary depth of a hypothetical finite-depth atmosphere, while the former does not depend on the depth of the atmosphere.

In the modified wave–CISK models, the zonal velocity is dominated by wavenumber one, with the vertical velocity confined to a single concentrated cell. This result suggests that Kelvin and gravity waves generated by convective heating are nonlinearly organized into a large-scale coherent structure due to the conditional heating. The concentration is qualitatively in agreement with observed superclusters (e.g., Nakazawa 1988); however, the appearance of only one supercluster-scale precipitation cell is contrary to observations.

To prevent the rapid growth of small-scale waves inherent in wave–CISK, Miyahara (1987) artificially suppressed small-scale waves by spatial filtering, while Itoh (1989) invoked a critical-convergence condition that allows convective heating to occur only above a certain critical value of large-scale convergence. Xie (1991) demonstrated through use of a high-resolution wave–CISK model with positive-only conditional heating that the wavenumber one structure of the zonal velocity appearing in an R15 model becomes a multiwavenumber structure in an R63 model, when using an ordinary value for diffusion. This result suggests that the wavenumber-one structure found by Lau and Peng (1987) probably depends on the resolution as well as the given values of the heating parameter and horizontal diffusion.

### *e. Evaporation–wind feedback instability theory*

As a new approach to explain intraseasonal oscillations, Neelin et al. (1987) and Emanuel (1987) proposed the evaporation–wind feedback theory. It was assumed that convective heating is not only proportional to moisture convergence but also to evaporation, which is in turn proportional to the surface wind. Instability was found to occur in 20–40-day eastward-moving Kelvin waves. However, the growth rate was found to increase with wavenumber in the absence of conditional heating.

Neelin et al. (1987) demonstrated, with the use of an ocean-surface R15 climate model with convective adjustment, that 20–40-day oscillations were significantly reduced when the surface wind was not allowed to fluctuate. Nevertheless, these oscillations still remained in the model. This result suggests that 20–40-day oscillations can be generated, to some extent, by wave–CISK or other mechanisms and can be greatly enhanced through the evaporation–wind feedback process. This result does not, however, exclude the possibility that these oscillations can be primarily generated by evaporation–wind feedback instability and somewhat enhanced by wave–CISK or other mechanisms.

Recently, Yano and Emanuel (1991) reexamined this theory by allowing vertical propagation. It was found that short tropospheric waves were strongly damped due to the energy loss to the stratosphere, the most unstable mode shifting to low wavenumbers. On the other hand, Xie (1991), using a two-level nonlinear model without the stratosphere, showed that evaporation–wind feedback instability with conditional heating simulated a wavenumber-one zonal velocity structure and multiple precipitation cells. The unstable wave was characterized by the temperature being in phase with evaporation while being nearly 90 degrees out of phase with the precipitation and vertical velocity.

The in-phase relationship implies an efficient energy generation by the part of the precipitation due to evaporation, while the quadrature relationship implies an inefficient energy generation by a portion of the precipitational heating directly related to moisture convergence. The quadrature phase relationship results from the vertical velocity being in quadrature with the surface zonal velocity, which in turn is in phase with evaporation and temperature. In contrast, unstable wave–CISK waves are characterized by temperature being nearly in phase with convective heating and vertical velocity (Hayashi 1970).

## 3. Model and observed data

The main model used in the present paper is a nine-level GFDL spectral general circulation model with rhomboidal truncation at zonal wavenumber 30, the effective latitudinal grid resolution being 2.25 degrees. The physical processes include moist convective adjustment (Manabe et al. 1965), surface hydrology, a planetary boundary layer, and radiational processes. Also included are orography, an imposed annual cycle of insolation, climatological sea surface temperatures, and climatological cloudiness. Detailed descriptions of this model are given by Manabe et al. (1979) and Gordon and Stern (1982). The data used for the present study were taken from the model that had been integrated over nine years. The model data were analyzed by the use of space–time spectrum and filter analyses.

For comparison purposes, the same analyses were performed on the four-dimensional assimilation dataset processed by the use of a general circulation model at the European Centre for Medium-Range Weather Forecasts (ECMWF). For model and data details, see Bengtsson et al. (1982), Hollingsworth et al. (1985, 1986), and Trenberth and Olson (1988). The periods these data cover are December 1978 through November 1979 (the FGGE year) and January 1980 through December 1987. In the present paper, these data will be referred to as "observed data," although they are, to some extent, model dependent. Hereafter, the term "FGGE data" refers to the ECMWF data for the FGGE year.

Space–time spectral analysis (see Hayashi 1982) results in wavenumber-frequency spectral distributions as well as the statistical space–time structure of the eastward- and westward-moving components for a given wavenumber and period. Space–time spectra were estimated by the maximum entropy method (see Hayashi 1982). Since the present spectral analysis makes use of an entire year of data, it is not necessary to remove seasonal cycles prior to the spectral analysis.

By the use of space–time filter analysis (see Hayashi and Golder 1986), the data, which are filtered for a given wavenumber and period range, can be composited, being phase shifted for the eastward or westward phase velocities. The compositing acts to enhance the chosen eastward or westward component, depending on the direction of the phase shift. Time filtering was accomplished by the use of a recursive digital filter (see Murakami 1979). The frequency response of a 40–50-day bandpass filter, for example, is designed in such a way that the amplitudes at 40- and 50-day periods are halved, while it is almost unchanged at a period of 45 days.

## 4. Wave characteristics

### *a. Wavenumber-frequency distributions*

Figure 1 displays the 205-mb wavenumber–frequency distributions for the model years 1–9 of the space–time power spectral density of the R30 zonal velocity that was latitudinally averaged over 10°N–10°S. The nine-year average spectra (upper-left panel) exhibit two intraseasonal-scale wavenumber-one spectral peaks with comparable magnitudes at eastward-moving periods of 40–50 and 25–30 days.

These two peaks can be detected in most of the individual yearly spectra. For several individual years, one peak is dominant over the other, while during other years the magnitudes are comparable. For example, the 25–30-day peak is dominant during year 5, while the 40–50-day peak is dominant during year 7, with comparable magnitudes found in year 1.

The corresponding 200-mb spectral distributions of the ECMWF data during the years 1979–87 are shown in Fig. 2. The nine-year average spectra (upper-left panel) exhibit a wavenumber-one spectral peak at eastward-moving periods of 50–60 days, its magnitude being comparable to that of the averaged simulated 40–50-day peak. For the individual years, a major peak occurs around 40–50 days during 1979, 1983, and

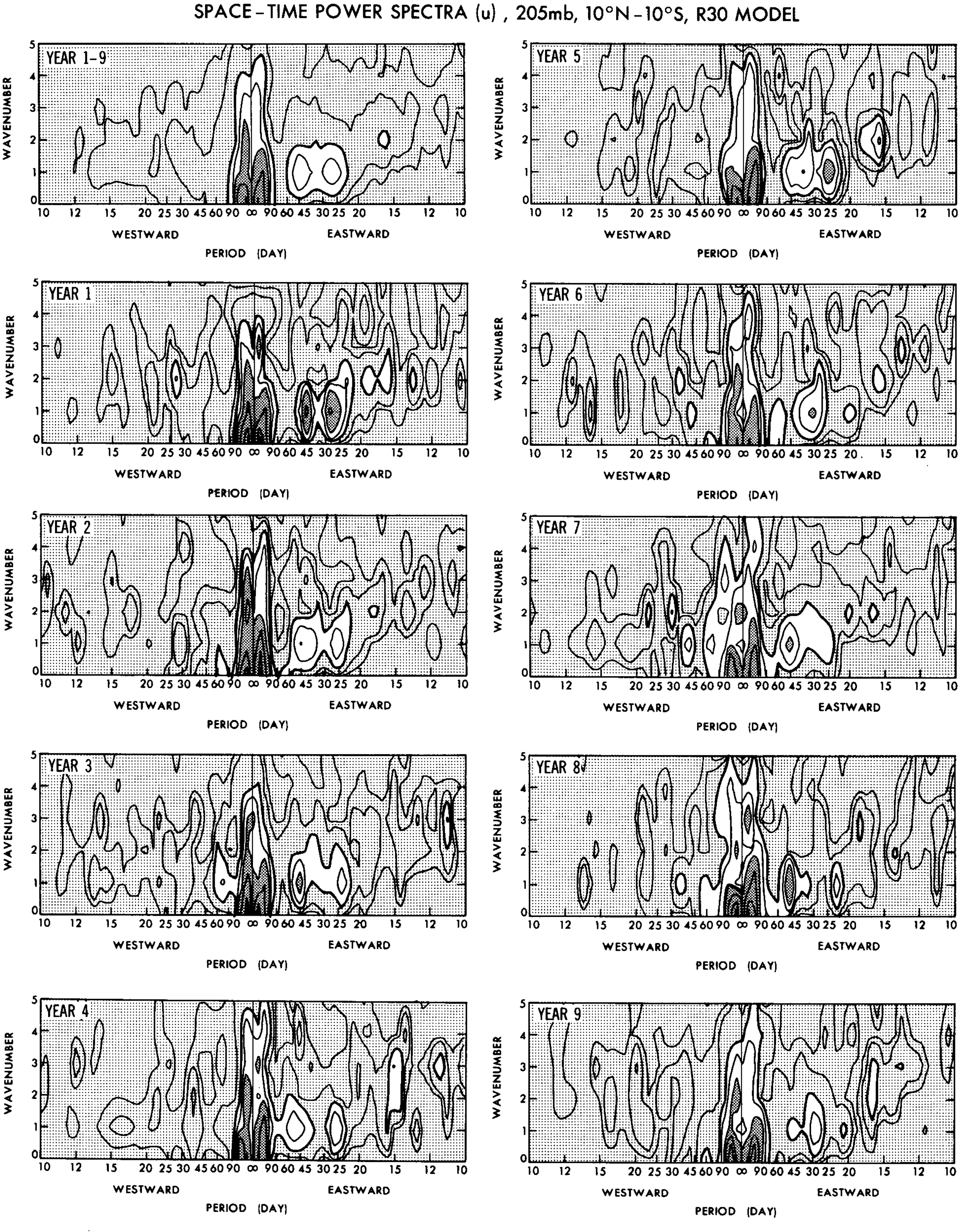

FIG. 1. Wavenumber–frequency distributions (205 mb) of the space–time power spectral density of the R30 model zonal velocity averaged over 10°N–10°S for the nine-year average (upper-left panel) and individual model years (year 1–9). The wavenumber range shown is 0–5, while the period domain is 10 days westward to 10 days eastward. Contour values are 1, 2, 5, 10, 20, 50, and 100 (10 $m^2 s^{-2}$ day). Dark shade indicates values greater than 20, while light shade indicates values less than 5.

SPACE-TIME POWER SPECTRA (u), 200mb, 10°N–10°S, ECMWF

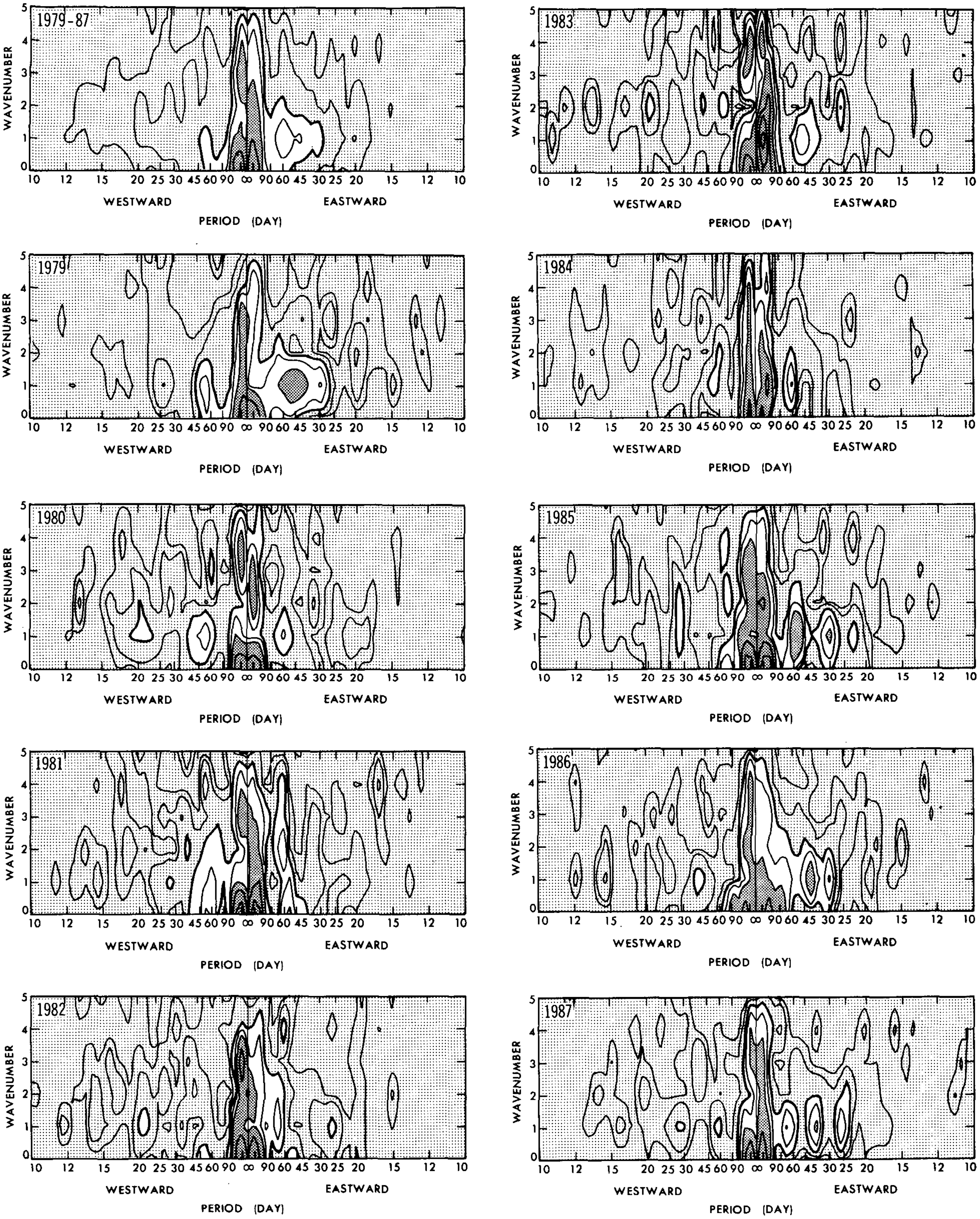

FIG. 2. As in Fig. 1 except for the ECMWF data at 200 mb for the years 1979–87.

1986, while over the 50–60-day range during the years 1980, 1981, 1982, 1984, and 1985. In addition, a minor peak is detected around 25–30 days during the years 1979, 1982, 1985, 1986, and 1987, although this peak is obscured in the nine-year average.

Overall, the ECMWF spectra exhibit a stronger interannual variability than the model spectra, since there is no interannual variability in the model's prescribed sea surface temperatures. Kuma (1990a) detected a quasi-biennial oscillation in the intensity of intraseasonal oscillations in 25 years of data observed at Singapore. It is difficult, however, to detect this oscillation in the space–time spectra of the nine-year ECMWF dataset. There is also the possibility that this oscillation might be localized in the Singapore area. The interactions between the intraseasonal oscillations and the El Niño–Southern Oscillation events were discussed by Lau and Chan (1986b, 1988) and Zebiak (1989).

To facilitate the comparison between the simulated and observed spectra, the frequency-spectral distributions of the wavenumber-one space–time power spectral density are plotted in Fig. 3 for the R30 model (nine-year average), the ECMWF data (1979–87 average), and the FGGE data (1979). In this figure, the seasonal variation was removed from the data prior to the spectral analysis. The climatological seasonal cycles were estimated by compositing the data over nine years and further smoothing the composite by a 61-day running mean. The 90–360-day variances are substantially reduced by this procedure, confirming that these variances are primarily due to climatological seasonal cycles.

Similar to the results found in previous papers (Hayashi and Golder 1986, 1988), the simulated (thick solid curve) 40–50-day spectral peak averaged over nine years is much weaker than the corresponding FGGE peak (dashed curve) and somewhat weaker than the 1985 and 1986 peaks (not shown in Fig. 3). On the other hand, the simulated 25–30-day peak is in agreement with the corresponding FGGE peak as well as with the 1985, 1986, and 1987 peaks (not shown in Fig. 3). When the simulated peaks are compared to the observed (thin solid curve) nine-year averaged peaks, however, the simulated 40–50-day peak is as strong as the 50–60-day peak, whereas the simulated 25–30-day peak is much stronger than that observed.

### *b. Longitudinal distributions*

It is possible that the 40–50- and 25–30-day periods are due to different local phase speeds that depend on the local time-mean flow. Figure 4 shows the longitude–frequency distributions of the nine-year averaged time–power spectra of the simulated (205 mb) and observed (200 mb) zonal velocity. The simulated zonal-velocity spectra attain maxima around 60°–90°E and 30°–120°W, for both the 40–50- and 25–30-day periods. These periods do not vary greatly from region to region. Therefore, the 40–50- and 25–30-day oscillations are, on the average, not longitudinally isolated from each other.

The corresponding observed spectra show similar features, except that the 50–60-day oscillations overshadow the 25–30-day oscillations. Inspection of lon-

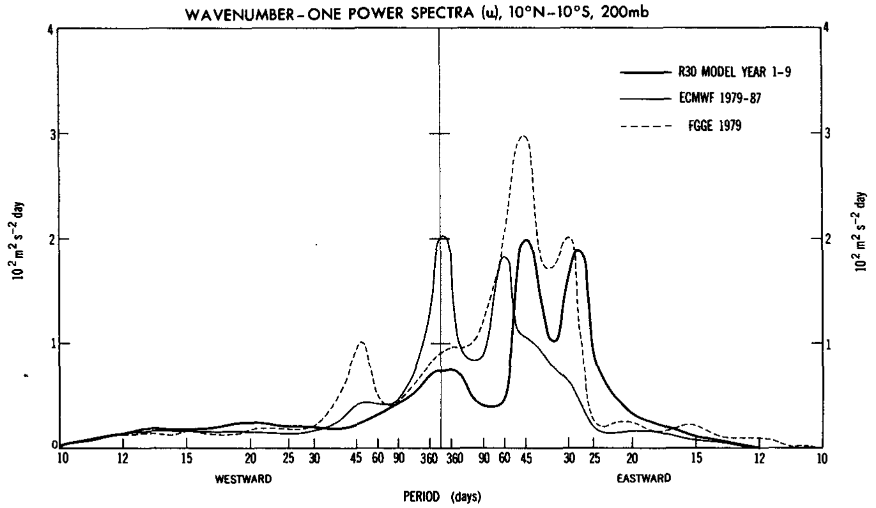

FIG. 3. Frequency–spectral distribution of the wavenumber-1 component space–time power spectral density (100 $m^2$ $s^{-2}$ day) of zonal velocity averaged over 10°N–10°S for the R30 model at 205 mb, year 1–9 (thick curve), the ECMWF data at 200 mb, 1979–87 (thin curve), and the FGGE data at 200 mb, 1979 (dashed curve). Seasonal variations were removed prior to the spectral analysis.

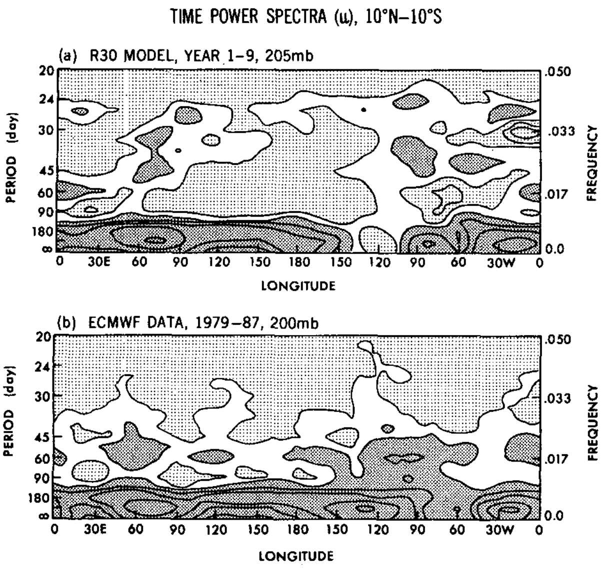

FIG. 4. Longitude–frequency distributions of the time-power spectral density (year 1–9) of the zonal velocity averaged between 10°N–10°S of the R30 model (a) at 205 mb and the ECMWF data 1979–87 (b) at 200 mb. Contours 20, 50, 100, 200, 500, and 1000 (10 $m^2 s^{-2}$ day). Dark shade > 50, light shade < 20.

gitude–frequency sections for the individual years (not illustrated) indicate that the two oscillations tend to have large amplitudes in the same regions, not being longitudinally isolated. However, it should not be concluded from the time spectra that the amplification always occurs at the same longitudes. Inspection of longitude–time sections (not illustrated) indicates that the intermittent amplification of the simulated and observed oscillations can occur at any longitude.

### c. *Temporal distributions*

It is possible that the 40–50- and 25–30-day periods result from different phase speeds due to the seasonal variation in the zonal flow. There is also the possibility that the two periods result from a seasonal frequency modulation of an intrinsic 35-day period. The presence of a semiannual cycle in the basic state will give additional 29.3- and 43.4-day periods, which correspond to the sum and difference of 1/35 and 1/180 $day^{-1}$ frequencies, respectively. In this case, the 40–50- and 25–30-day oscillations will jointly grow and decay. Moreover, if there is a systematic phase relation between the two oscillations, the 25–30-day oscillations can be enhanced by the 40–50-day oscillations at every 45th day.

Figure 5 shows the time distribution of the frequency-filtered wavenumber-one Fourier cosine coefficient of the 200-mb zonal velocity that was averaged between 10°N and 10°S for the R30 model (year 4) and ECMWF data (1985). The model and data indicate that the 40–50- and 25–30-day oscillations appear strongly during different seasons of the year. The growth and decay occur in a different manner from year to year (not illustrated), however, and are not primarily due to the seasonal modulation of the amplitude.

The seasonal modulation is not easily detected in individual years, since it is very slow compared with the intraseasonal time scale. The seasonal modulation of observed intraseasonal oscillations can be found in time-varying spectra averaged over many years (Madden 1986; Gutzler and Madden 1989). The seasonal modulation of time-varying space–time spectra of 10–20-day Kelvin waves and 3–5-day mixed Rossby-gravity waves simulated by a GFDL model can be found in Hayashi and Golder (1980).

Inspection of the time distributions for the other individual years shows (not illustrated) that no systematic relationship can be found between the amplifications of the two oscillations. They grow and decay independent of each other, one occasionally dominating the other, which is consistent with the intermittent regular phase propagations of observed outgoing longwave radiation (Murakami 1987, 1988). Moreover, no systematic phase relationship can be found between the two oscillations, indicating that the 40–50-day oscillations do not systematically modulate the 25–30-day oscillations.

## 5. Planetary-scale structure

Intraseasonal oscillations are associated with three structures: a planetary-scale structure, a supercluster-

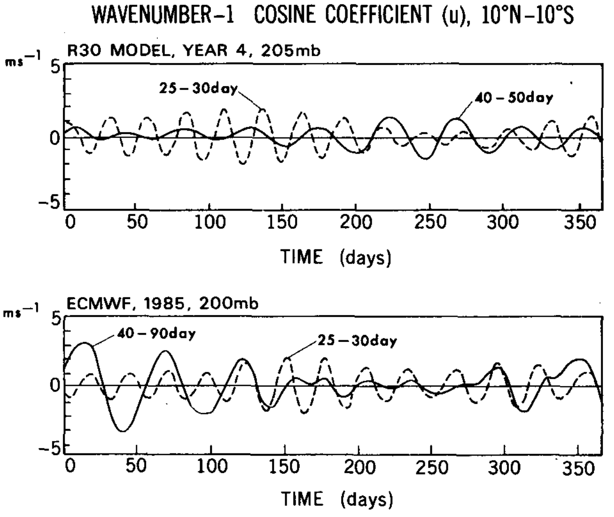

FIG. 5. Time distribution of the frequency-filtered wavenumber-one cosine coefficient ($m s^{-1}$) of zonal velocity averaged between 10°N–10°S. The upper panel represents the R30 model (year 4) at 205 mb, 40–50-day filtered (solid curve) and 25–30-day filtered (dashed curve). The lower panel represents the ECMWF data (1985) at 200 mb, 40–90-day filtered (solid curve) and 25–30-day filtered (dashed curve).

scale structure, and a regional structure. The planetary-scale structure, which propagates globally, can essentially be described by the wavenumber-one component. The supercluster-scale structure, which is characterized by its concentrated vertical velocity propagating globally, consists of wavenumber 5–10 components. The regional structure, which depends on location, consists of numerous wavenumber components. In this section, the planetary-scale structure is analyzed, while the global and regional propagations of planetary and supercluster scales are described in section 7.

### *a. Wave patterns*

Figure 6 displays 200-mb longitude–latitude sections of the wavenumber-one, 40–50-day filtered wind vectors and geopotential height contours of the FGGE data. The data have been composited over a period of one year along the longitude–time isoline of an eastward (Fig. 6a) and westward (Fig. 6b) phase velocity of 10.3 m $s^{-1}$ in order to enhance the eastward- and westward-moving components having 45.0-day periods, respectively.

Near the equator, the eastward-moving composite exhibits a Kelvin mode pattern (see Fig. 8 of Matsuno 1966). This pattern is characterized by wind vectors directed parallel to the equator, the zonal component being in phase with geopotential heights near the equator. Away from the equator, the composite exhibits Rossby mode vortices that are characterized by the wind vectors being directed along geopotential height contours. This pattern is similar to that found in the GFDL FGGE and R30 model data (Hayashi and Golder 1986, 1988). This Kelvin–Rossby mode pattern was also reproduced by a thermal-forcing model having an imposed eastward-moving heat source (Hayashi and Miyahara 1987).

In contrast, the westward-moving composite (Fig. 6b) exhibits only Rossby mode patterns. The planetary-scale tropical intraseasonal oscillations can essentially be represented by these eastward- and westward-moving wavenumber-one components and the wavenum-

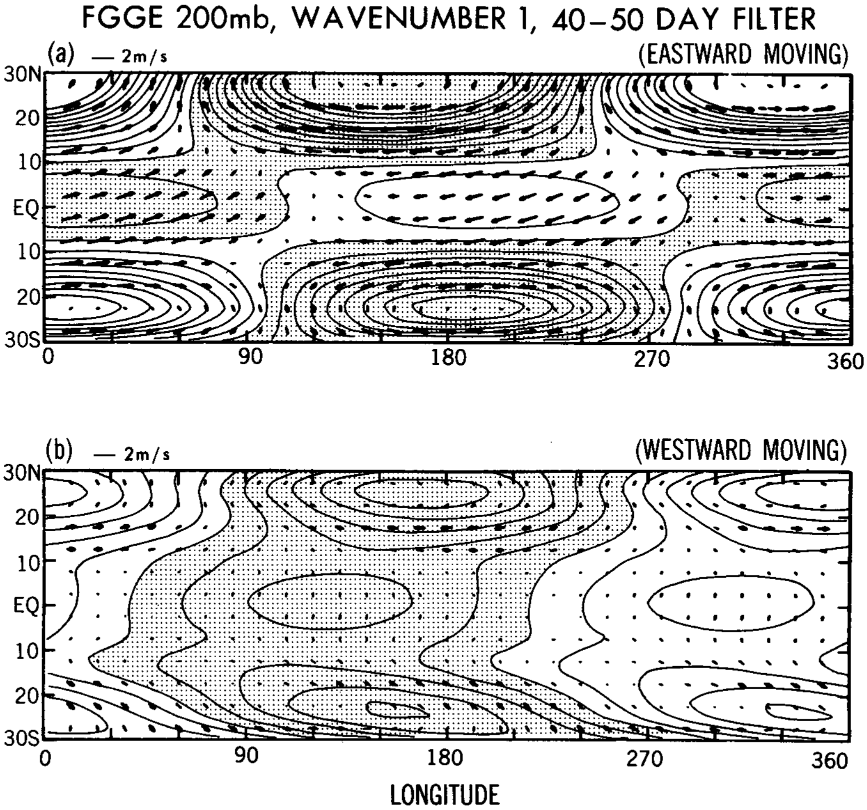

FIG. 6. Longitude–latitude sections (FGGE data, 200 mb) of the wavenumber-one, 40–50-day filtered wind vectors and geopotential height contours. The filtered data have been composited over one year along the longitude–time isoline of 10.3 m $s^{-1}$ (a) eastward and (b) westward phase velocities. The contour interval is 1 m. Shading indicates positive values. The horizontal bar indicates the magnitude of the zonal component of the wind vectors. The latitudinal scale and the meridional component have been enlarged by a factor of 2 relative to the longitudinal scale and the zonal component, respectively.

ber-zero (zonal mean) component. The space–time spectra of the geopotential height indicate (not illustrated) comparable eastward and westward propagation near the equator. Away from the equator (10°N–30°N, 10°S–30°S), the spectra indicate (not illustrated) eastward propagation for planetary-scale intraseasonal oscillations and westward propagation for high wavenumber–frequency components.

Figure 7 is the same as Fig. 6a (eastward-moving composite) except for (a) the 205-mb R30 model data (year 2) filtered for periods 40–50 days and (b) the 200-mb ECMWF data (1985) filtered for periods 40–90 days. The R30 model exhibits a Kelvin–Rossby wave pattern similar to that found in the FGGE data. In contrast, the geopotential height during 1985 is more than 90 degrees out of phase with the zonal velocity near the equator, being contrary to the Kelvin mode. This phase difference varies between 90 and 180 degrees from year to year during the non-FGGE years (not illustrated). The distortion of the Kelvin-wave structure is consistent with the observational analyses of Nishi (1989) and Hsu et al. (1990).

The individual wavenumber components of a linear Kelvin mode should be associated with an in-phase relationship between the zonal velocity and geopotential height, since the observed phase speed relative to the basic flow is eastward [see Eq. (A6) in the Appendix]. The observed equatorial zonal flow is not strong enough to reverse the relative phase speed. This phase relationship does not hold for the multiple-wavenumber patterns of Gill (1980), Yamagata and Hayashi (1984), and Lau and Lim (1982), or the single-wavenumber pattern of Matsuno (1966), which is strongly affected by friction.

Van Tuyl (1987) showed that the nonlinear Kelvin mode is associated with a quadrature phase relationship due to nonlinear advection. The observed distortion might be due to the nonlinear advection by high-wavenumber components that result from localized convective heating. In the FGGE year, the global propagation of divergence has been clearly observed (Lorenc 1984; Krishnamurti et al. 1985). When the convective heating is not well confined, the local nonlinear advection can be small. The distortion might also be due to the vertical transport of momentum by small-scale transient gravity waves and cumulus convection, which is not parameterized in the present model.

Figure 8 is the same as Fig. 7 except for near the

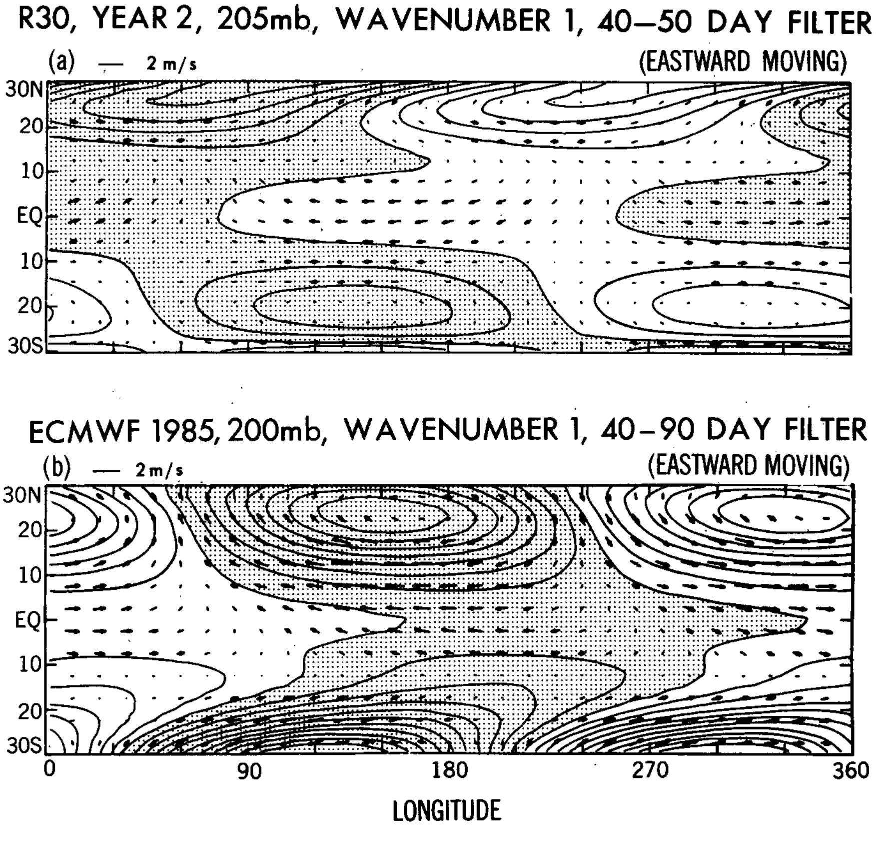
R30, YEAR 2, 205mb, WAVENUMBER 1, 40–50 DAY FILTER

ECMWF 1985, 200mb, WAVENUMBER 1, 40–90 DAY FILTER

FIG. 7. As in Fig. 6 except for (a) the R30 model with a 40–50-day filter at 205 mb for year 2, and (b) the ECMWF data with a 40–90-day filter at 200 mb for 1985.

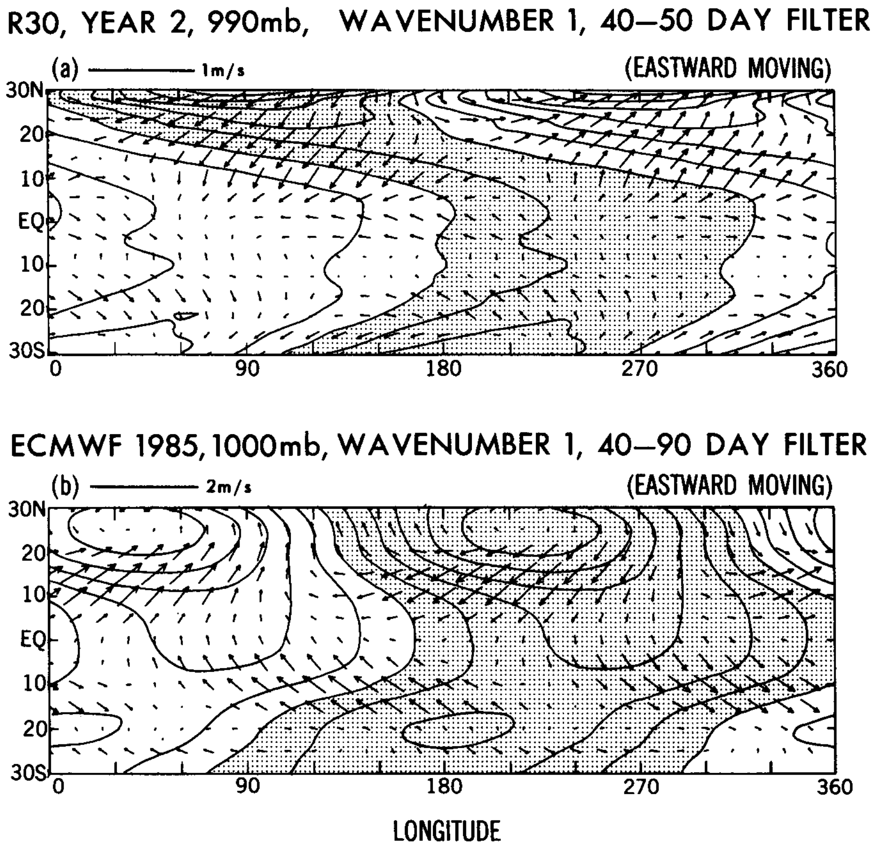
R30, YEAR 2, 990mb, WAVENUMBER 1, 40–50 DAY FILTER

ECMWF 1985,1000mb, WAVENUMBER 1, 40–90 DAY FILTER

FIG. 8. As in Fig. 7 except at the 990-mb (R30 model) and 1000-mb (ECMWF data) levels.

surface. The simulated and observed wave patterns do not resemble the Kelvin mode. In particular, the zonal velocity and geopotential oscillations near the equator are nearly 90 degrees out of phase, while wind vectors away from the equator cross the geopotential height contours. This is probably due to the effect of vertical diffusion, as shown theoretically by a thermal-forcing model with and without surface stress (Hayashi and Miyahara 1987).

The frictionally induced meridional velocity plays an important role in low-level convergence. When the horizontal resolution of the model is increased, frictional convergence will be enhanced more efficiently for the 40–50-day oscillations than 25–30-day oscillations, since frictional convergence is more efficient in lower-frequency oscillations (Hayashi 1971a).

### *b. Latitudinal structure*

Figure 9a shows the nine-year R30 latitudinal distributions of the normalized space–time amplitude, phase difference, and coherence of the zonal velocity ($u$) and geopotential ($\phi$) at 205 mb. These distributions are for wavenumber one at an eastward-moving period of 45.0 days. Here, the phase and coherence are calculated with reference to $u$ at the equator.

It is seen that both $u$ and $\phi$ attain a local maximum

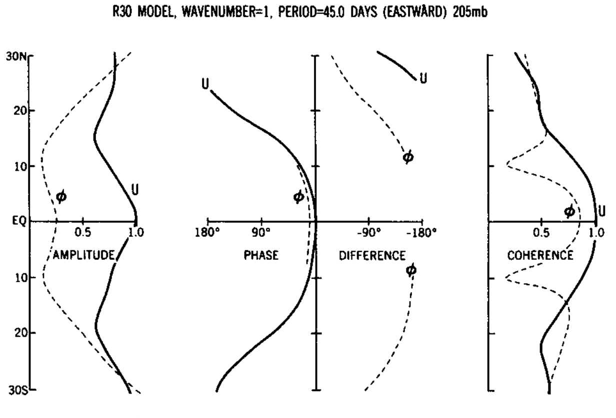
R30 MODEL, WAVENUMBER=1, PERIOD=45.0 DAYS (EASTWARD) 205mb

FIG. 9a. Latitudinal distributions (R30 model over years 1–9) of the normalized space-time amplitude, phase difference, and coherence (wavenumber one, period 45.0 days, eastward moving) of the zonal velocity (solid) and geopotential height (dashed) at 205 mb. The phase and coherence are with reference to the zonal velocity at the equator.

amplitude over the equator and are nearly in phase between 10°N and 10°S, being consistent with the equatorial Kelvin mode. Outside this latitude band, $u$ and $\phi$ are associated with amplitudes increasing with latitude and an out-of-phase relationship, being consistent with the Rossby mode. Also, the geopotential height displays an abrupt 180 degree phase shift across the 10° latitudes, while the zonal velocity is associated with a gradual westward phase tilt with latitude. For the westward-moving component (not illustrated), $u$ and $\phi$ do not attain a local maximum over the equator and are nearly out of phase close to the equator, being consistent with the Rossby mode.

Figure 9b is the same as Fig. 9a except for the period of 25.7 days. The latitudinal amplitude and phase structures of the simulated 25–30-day oscillation are very similar to those of the simulated 40–50-day oscillation, in spite of the large difference in their periods. The eastward-moving components of both oscillations are consistent with the Kelvin mode near the equator and the Rossby mode away from the equator, while the westward-moving components (not illustrated) are dominated by Rossby modes.

Figure 10a (period = 45.0 days) is the same as Fig. 9a except for the FGGE year at 200 mb. As in the simulation, the Kelvin and Rossby mode phase structures can be seen. The zonal velocity does not exhibit a maximum amplitude over the equator, however, being contrary to the linear Kelvin mode. During non-FGGE years (1980–87) as in Fig. 10b (period = 60.0 days), the zonal velocity does not exhibit a maximum amplitude over the equator. Moreover, $u$ and $\phi$ close to the equator are nearly out of phase, being contrary to the linear Kelvin mode. The low coherence between $u$ and $\phi$ near the equator is consistent with the fact that the phase difference varies from year to year.

### c. Vertical structure

Figure 11a shows the nine-year R30 vertical distributions of the normalized space–time amplitude, phase, and coherence (wavenumber one, period 45.0 days eastward) of the zonal velocity ($u$), temperature ($T$), vertical pressure velocity ($\omega$), and convective heating ($Q$) averaged over 10°N–10°S. The phase and coherence were calculated with reference to $-\omega$ at the 515-mb level.

The zonal velocity attains amplitude maxima around the 205-mb and 680-mb levels, with a 180 degree phase reversal between these levels. The vertical pressure velocity attains its maximum amplitude at the 515-mb level. At 205 mb, $u$ and $-\omega$ are nearly 90 degrees out of phase, being consistent with the zonal propagation of a longitudinal cell-like structure. Unlike the zonal velocity, the phase line of the vertical velocity ($-\omega$) tilts westward with height below the 500-mb level, resulting in $u$ and ($-\omega$) being nearly 180 degrees out of phase near the surface.

This tilt is probably due to boundary-layer meridional convergence (see Hayashi and Golder 1988, Fig. 14), which has also been reproduced in the results of theoretical models by Hayashi and Miyahara (1987, Fig. 8) and Wang and Rui (1990). The 180 degree

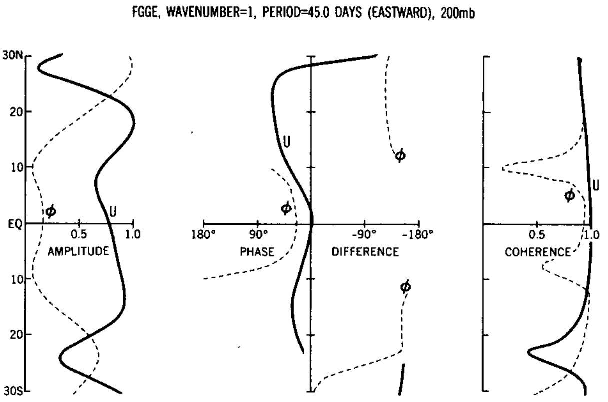

FIG. 10a. As in Fig. 9a except for the FGGE year at 200 mb.

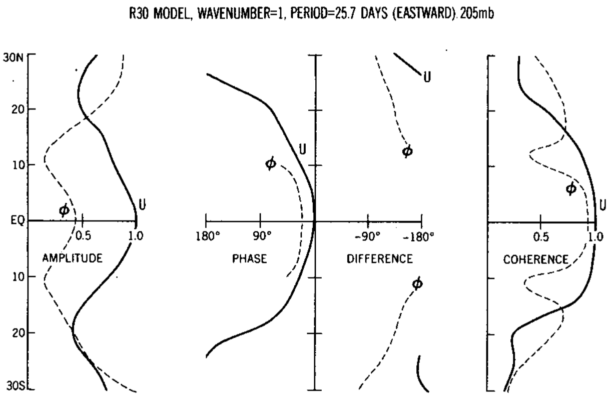

FIG. 9b. As in Fig. 9a except for a period of 25.7 days.

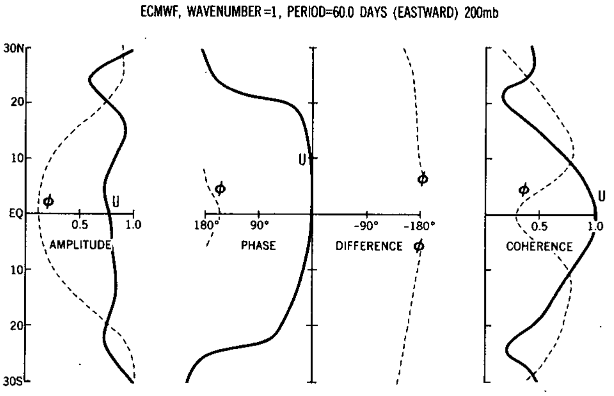

FIG. 10b. As in Fig. 9a except for the ECMWF data (over 1980–87) at 200 mb and a period of 60.0 days.

out-of-phase relationship between the low-level vertical velocity and the surface wind is consistent with the in-phase relationship found between the low-level convergence and evaporation in the model (not illustrated). This phase relationship implies that wave–CISK and evaporation–wind feedback act conjointly in the presence of frictional convergence.

Figure 11a also indicates that the convective heating attains its maximum amplitude around the 515-mb level and is nearly in phase with the vertical velocity, both tilting westward with height below this level. The abrupt 180° phase shift between the 940- and 990-mb levels results from the upward heat transport produced by the model's convective adjustment. The vertical tilt of convective heating is not considered in wave–CISK theories that assume that the parameterized convective heating has no vertical tilt.

It should be noted that the 350-mb temperature is nearly in phase with both the convective heating and vertical velocity, indicating that eddy potential energy is generated and converted into eddy kinetic energy, in agreement with the observed energy conversion (Murakami et al. 1984; Krishnamurti et al. 1985; Chen 1985).

Figure 11b displays the same distributions as in Fig. 11a except for the periods of 25.7 days. It should be noted that Fig. 11b bears a striking resemblance to Fig. 11a in spite of the large difference in the selected periods. When carefully inspected, however, the 25.7-day zonal velocity amplitude exhibits a slightly greater increase in amplitude from the 830-mb to 205-mb levels than the 45.0-day zonal velocity amplitude, while the 25–30-day convective heating amplitude exhibits a slightly greater increase with height in the lower troposphere. The dissimilar vertical distributions of the 40–50- and 25–30-day amplitudes result in different relative magnitudes of their spectral peaks at various levels, as will be shown in section 7.

Figure 12 shows the corresponding vertical distribution of the ECMWF data (1980–87) for eastward-moving (a) 60.0-day and (b) 30.0-day periods. The vertical distributions of the observed amplitude and phase are similar to those of the model; however, the vertical pressure velocity attains its maximum at the somewhat higher level of 300 mb. Also, the vertical velocity exhibits a stronger westward tilt below 500 mb. Although convective heating was not available in the ECMWF dataset, the vertical distribution of the vertical velocity suggests that the observed convective

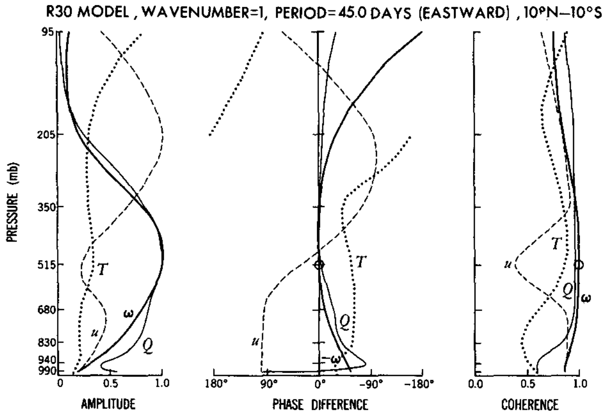

FIG. 11a. Vertical distributions (R30 model over years 1–9) of the normalized space–time amplitude, phase difference, and coherence (wavenumber one, period 45.0 days, eastward moving) of the zonal velocity ($u$, dashed), temperature ($T$, dotted), vertical pressure velocity ($-\omega$, thick solid), and convective heating ($Q$, thin solid) averaged between 10°N and 10°S. The phase and coherence are with reference to the 515-mb vertical pressure velocity, which is indicated by an open circle.

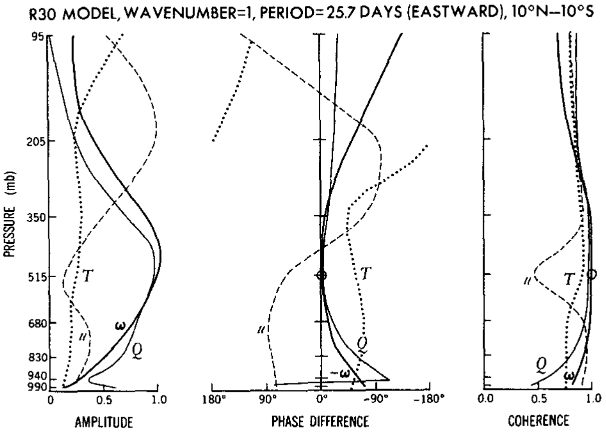

FIG. 11b. As in (a) except for the eastward-moving period of 25.7 days.

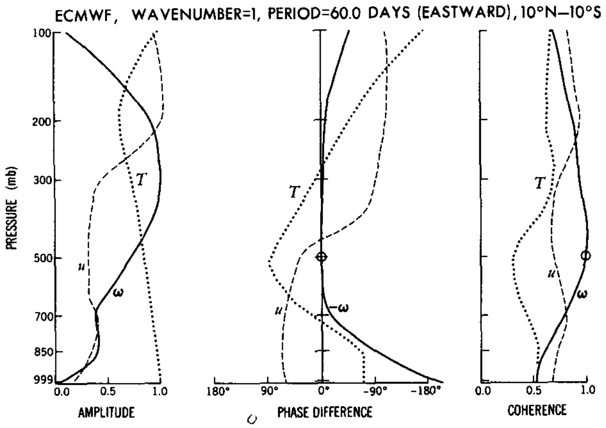

FIG. 12a. As in Fig. 11a except for the ECMWF data (over 1980–87), an eastward-moving period of 60.0 days, and a reference level of 500 mb. Convective heating data are not available for the ECMWF data.

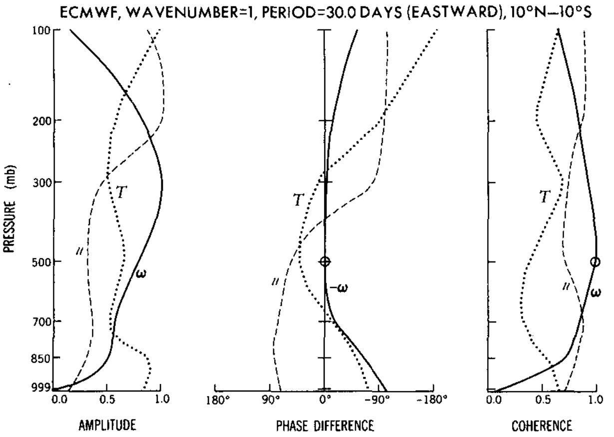

FIG. 12b. As in Fig. 12a except for an eastward-moving period of 30.0 days.

heating should attain its maximum at a higher level than the simulated convective heating.

The ECMWF data also indicate that the 300-mb temperature is nearly in phase with the vertical velocity. As in the model, the 30.0-day zonal-velocity amplitude exhibits a slightly greater increase from the 850-mb to 200-mb levels than the 60.0-day oscillation.

## 6. Effects of higher vertical resolution

The previous section demonstrated that the 40–50- and 25–30-day oscillations have similar horizontal structure but exhibited some differences in their vertical structure. There is the possibility that several further differences in the vertical structure may arise when the vertical resolution of the model or the observed data is increased. The 25–30-day oscillations might appear primarily as stratospheric waves, since shorter-period Kelvin waves are theoretically associated with a larger vertical group velocity (Hayashi 1976), their energy propagating upward more efficiently.

To examine these possibilities, a brief analysis was performed on three years of data from a GFDL troposphere-stratosphere-mesosphere general circulation model. The model analyzed here—termed "SKYHI"—has a vertical resolution of about 1 km in the troposphere and stratosphere, and a latitudinal grid resolution of 3 degrees (N30). For details of the model, see Mahlman and Umscheid (1984). The data used in this spectral analysis were averaged between 10°N and 10°S, while the spectral results shown in the figure have been averaged over the three years.

Figure 13 shows the frequency-height distribution of the space-time power spectral density for the wave-

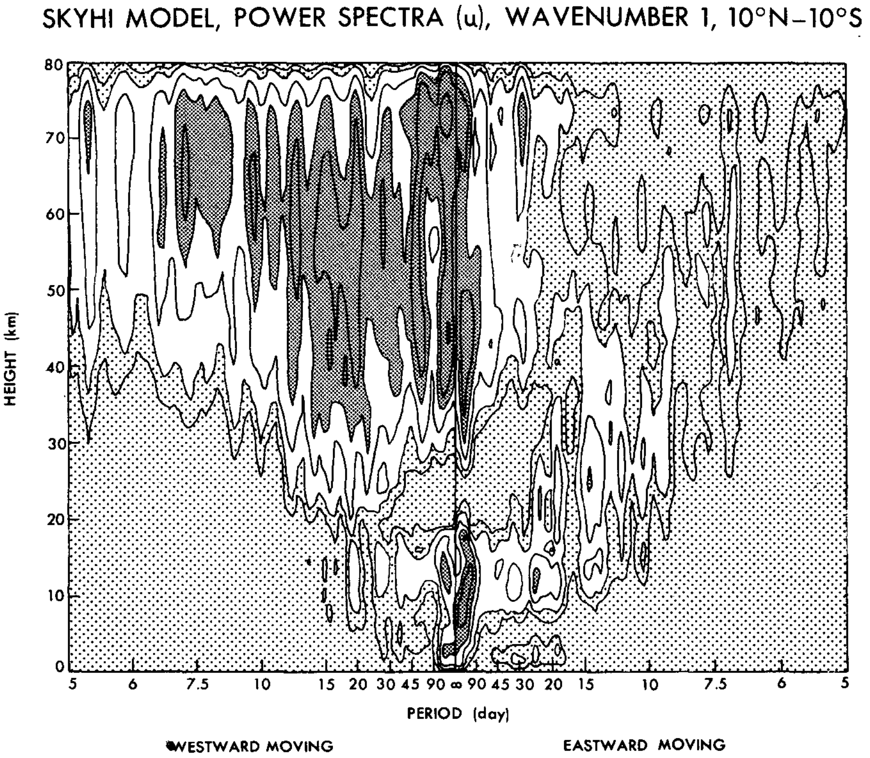

FIG. 13. Frequency-height distribution (N30 SKYHI model) averaged over three years of the space-time power spectral density (10 $m^2$ day) for the wavenumber-one zonal velocity averaged between 10°N and 10°S. Contours 1, 2, 5, 10, 20, 50, and 100 (10 $m^2$ day). Dark shade > 10; light shade < 2.

number-one component of the SKYHI zonal velocity. In the upper troposphere (around 12 km), spectral peaks are seen for eastward-moving periods near 40–50 and 25–30 days. The 40–50-day peak is confined to the troposphere, while the 25–30-day peak penetrates into the lower stratosphere. The 25–30 day oscillation essentially remains a tropospheric phenomenon, however, in spite of the increase in the vertical resolution. Although the 25–30-day peak appears stronger than the 40–50-day peak over the three years of data, these peaks will probably become comparable in the long-term average, if the model is integrated over many years.

In the upper troposphere and lower stratosphere, an eastward-moving 10–20-day peak can also be seen that corresponds to the stratospheric equatorial Kelvin wave discovered by Wallace and Kousky (1968). This wave was simulated in an 11-layer GFDL general circulation model (Hayashi 1974) and a corresponding ocean-surface model (Hayashi and Golder 1978). The 10–20-day peak appears more distinctly in the SKYHI model than the R30 model (not illustrated) probably due to the higher vertical resolution.

At higher levels, spectral peaks occur for higher eastward-moving frequencies. These peaks correspond to the upper-stratospheric 5–7-day Kelvin wave (Hirota 1979) and the mesospheric 3–4-day Kelvin wave (Salby et al. 1984). These waves were also simulated in an N18 SKYHI model (Hayashi et al. 1984). In the mesosphere, the spectra are dominated by westward-moving components, corresponding to observed external (or equivalent barotropic) Rossby modes (see Madden 1979).

Figure 14 displays the vertical distributions of the normalized space–time amplitude, phase difference, and coherence for the wavenumber-one component of the SKYHI zonal velocity for eastward-moving periods of 45.0, 25.7, and 15.0 days. The phase and coherence distributions are with reference to the zonal velocity at the 102-mb level. All three waves indicate a 180 degree phase reversal between the lower and upper troposphere. In the lower stratosphere (16–30 km), all three waves exhibit an eastward tilt with height, while the 15.0- and 45.0-day waves show the smallest and largest phase variations, respectively. The increase in the vertical phase tilt with increasing period is consistent with the Kelvin-wave dispersion relation (see Hayashi 1976, p. 190). The difference in the vertical wavelengths occurs only above the level of convective heating, since the actual vertical wavelength in the layer of heating is determined by the vertical scale of the heating rather than the intrinsic vertical wavelength.

These results suggest that the three oscillations differ in their intrinsic vertical wavelengths, although this difference cannot be detected in the nine-level R30 model. Each of these modes can be represented by a linear combination of several of the model's vertical normal modes. A vertical normal-mode expansion of the GFDL FGGE dataset can be found in Nogueś-Paegle et al. (1989). Above the SKYHI 30-km level, the 45.0- and 25.7-day oscillations appear to be associated with small vertical phase variations. This is probably due to the amplitude and phase of the eastward-moving components being contaminated by the westward-moving components that dominate the spectra.

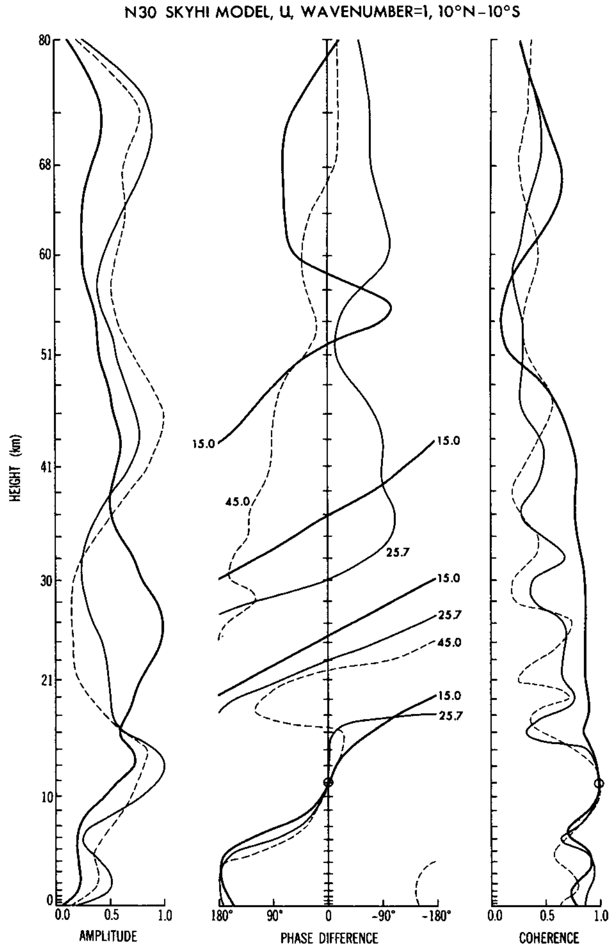

FIG. 14. Vertical distributions (N30 SKYHI model) averaged over three years of normalized space–time amplitude, phase difference, and coherence of the wavenumber-one zonal velocity averaged between 10°N and 10°S. The curves are drawn for eastward-moving periods of 45.0 (dashed), 25.7 (thin solid), and 15.0 (thick solid) days. The phase and coherence distributions are with reference to the 102-mb level. The tick marks indicate the vertical resolution of the model.

Figure 15 is the same as Fig. 14 except for tropospheric convective heating. (Note that the height coordinate extends to only 18 km.) The heights of maximum amplitudes for the 45.0-, 25.7-, and 15.0-day periods occur at 4.5, 5.5, and 6.5 km, respectively. The corresponding vertical velocity oscillations exhibit

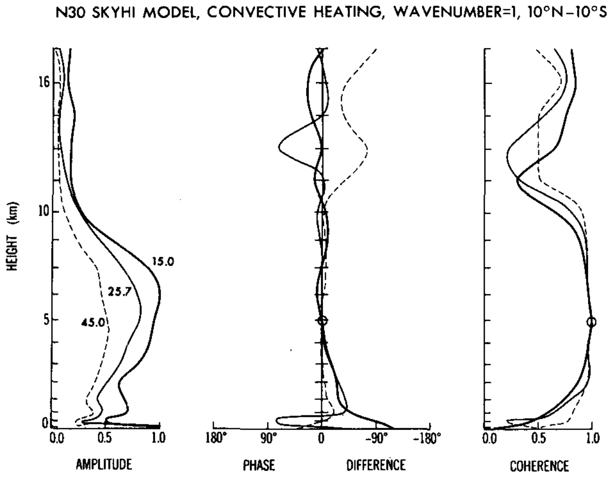

FIG. 15. As in Fig. 14 except for tropospheric convective heating at heights between 0 and 17 km.

similar vertical distributions of amplitude and phase (not illustrated).

According to wave–CISK theory (Hayashi 1970), the single vertical distribution of parameterized convective heating is associated with multiple unstable vertical modes, the lowest vertical mode being the most unstable among the unstable modes. The decrease of period with an increase in the depth of convective heating is qualitatively consistent with the most unstable vertical mode of the Kelvin wave, the periods being 10–20, 25–30, and 40–50 days for convective heating that has a maximum in the upper, middle, and lower tropospheres, respectively (see Takahashi 1987; Lau and Peng 1987; Sui and Lau 1989). If the three mid-tropospheric-dominated vertical distributions found in the SKYHI model are applied to a wave–CISK model, however, the resulting period of the most unstable wavenumber one Kelvin mode will be in the range of 25–30 days. It is therefore difficult to explain the occurrence of the three spectral peaks by wave–CISK theories.

It is, however, incorrect to interpret that the periods of the simulated oscillations are extremely sensitive to the vertical heat distributions, since these distributions are determined by the internal dynamics through convective adjustment. It is probably more appropriate to conclude that a vertical distribution is not sensitive to a given period. Even if the height of the 25–30-day convective heating was slightly lower, the period would not shift to a 40–50-day period. If all three vertical heat distributions were bottom heavy, however, the 10–20-, 25–30-, and 40–50-day periods would probably shift to 25–30, 40–50, and 80–100 days, respectively. The shift of period from 25–30 to 40–50 days is consistent with the most unstable vertical mode of wave–CISK theory.

## 7. Effects of geographical and seasonal variations

It was concluded in section 4 that the 40–50- and 25–30-day spectral peaks result neither from the advective modification of intrinsic phase speeds by different local basic flows nor from the nonlinear modulation of their intrinsic period by seasonal cycles. These conclusions can be confirmed by demonstrating that these oscillations appear even in an ocean-surface model without seasonal variation. This model can also be used to clarify the effects of sea surface temperature on the geographical distribution of precipitation oscillations and to isolate nonlinearly localized supercluster-scale oscillations from geographically localized planetary-scale oscillations.

The present ocean-surface model was constructed by replacing the surface of the original R30 model by an ocean surface having zonally uniform temperatures. The temperatures were taken from the January zonal-mean ocean temperatures of an R30 model with no mountains (illustrated by Fig. 2 of Hayashi and Golder 1981). The model was integrated over a period of three years with the insolation conditions fixed at their January mean values to remove the seasonal variation.

### *a. Planetary-scale oscillations*

Figure 16 shows the wavenumber–frequency distributions of the space–time power spectral density of the 205-mb zonal component averaged between 10°N and 10°S of (a) the original R30 model and (b) the ocean-surface R30 model. The original model exhibits 40–50- and 25–30-day peaks of comparable magnitude as was already shown in Fig. 1, while the ocean-surface model exhibits both 40–50- and 25–30-day peaks having different magnitudes. Although the ocean surface model indicates a stronger 25–30-day peak than a 40–50-day peak, these peaks will probably have comparable magnitudes if the model is integrated over many years, since the original model indicated stronger 25–30-day peaks in several individual years, as was also shown in Fig. 1. Both peaks appear much stronger in the ocean-surface model than in the original model. This is probably because precipitation is not geographically localized in the ocean-surface model.

Both models indicate that the spectra of the eastward-moving components are distributed along the dispersion lines of Kelvin waves, represented by the two thick lines. These lines are drawn in such a way as to pass through the wavenumber-one 45- and 27-day periods, corresponding to eastward phase speeds of 10 and 17 m s$^{-1}$, respectively. According to linear theory (e.g., Lindzen 1967; Lindzen and Matsuno 1968), different dispersion lines are associated with different intrinsic vertical wavelengths. Minor spectral peaks do not exactly fall on the two dispersion lines, probably due to nonlinear effects.

POWER SPECTRA ($u$), 205mb, 10°N–10°S

(a) ORIGINAL R30 MODEL

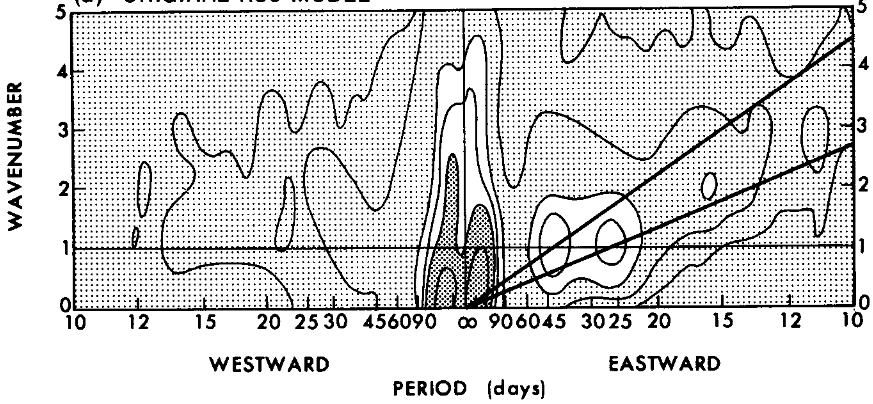

(b) OCEAN-SURFACE R30 MODEL

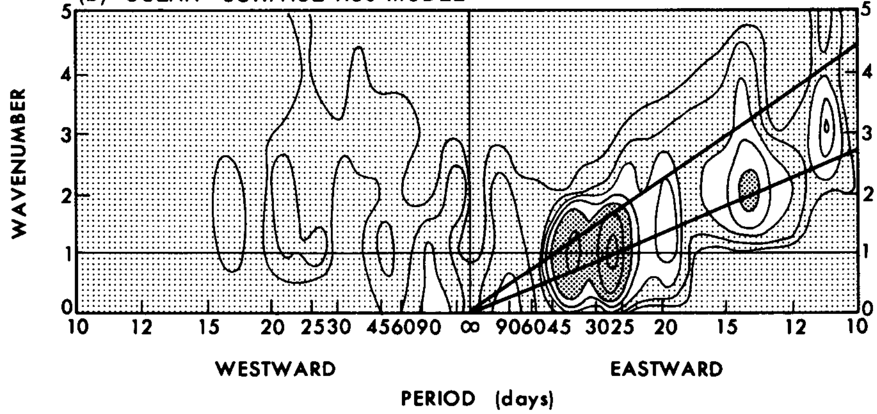

FIG. 16. Wavenumber-frequency distribution (205 mb) of the space–time power spectral density of the zonal velocity averaged over 10°N–10°S of (a) the original R30 model and (b) the ocean-surface R30 model. The slanted lines indicate Kelvin wave dispersion relations, corresponding to eastward phase speeds of 10 and 17 m $s^{-1}$ (see text). Contours 1, 2, 5, 10, 20, 50, and 100 (10.0 $m^2$ $s^{-2}$ day). Dark shade > 20, light shade < 5.

Figure 17 is the same as Fig. 16 except for the 830-mb zonal velocity. In contrast to the 205-mb spectra, the original model (a) indicates a somewhat stronger 40–50-day peak than a 25–30-day peak, while the ocean-surface model indicates comparable 40–50- and 25–30-day peaks, which are much stronger than those in the original model. The difference in the relative magnitudes of the two peaks between the 205- and 830-mb levels results from the different vertical distributions of the zonal velocity amplitudes, as was discussed in section 5.

To visualize the zonal propagation, Fig. 18 displays the longitude–time sections (830 mb, 10°N–10°S) of the sum of 40–50- and 25–30-day filtered wavenumber 0–1 components of (a) the zonal velocity and (b) geopotential height of the original model. This figure reveals that the zonal velocity is essentially an eastward-moving wave accompanied by a weak node and antinode, while the geopotential height is essentially a standing oscillation having a strong node and antinode.

For a spectral interpretation of the standing oscillation, Fig. 19a shows the space–time spectra of the geopotential height (830 mb, 10°N–10°S) of the original model. It can be seen that the 40–50- and 25–30-day standing wave oscillations consist of eastward- and westward-moving wavenumber-one components and a wavenumber-zero (zonal-mean) component. The latter component formally consists of eastward- and westward-moving components of the same magnitude.

The dominance of the wavenumber-zero component in the geopotential height spectra is consistent with the observed slow phase variation of pressure (Madden and Julian 1972; Maruyama 1982) and the thermal-forcing models of Yamagata and Hayashi (1984), Hayashi and Miyahara (1987), and Itoh and Nishi (1990). The wavenumber-zero component of geopotential height

POWER SPECTRA ($u$), 830mb, 10°N-10°S

(a) ORIGINAL R30 MODEL

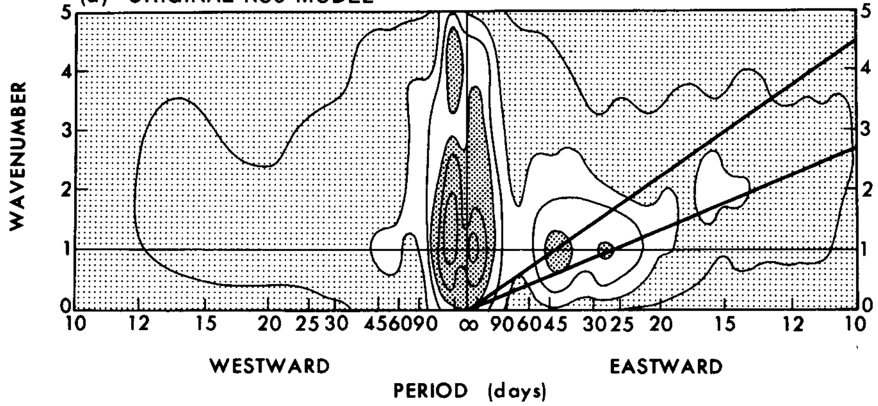

(b) OCEAN-SURFACE R30 MODEL

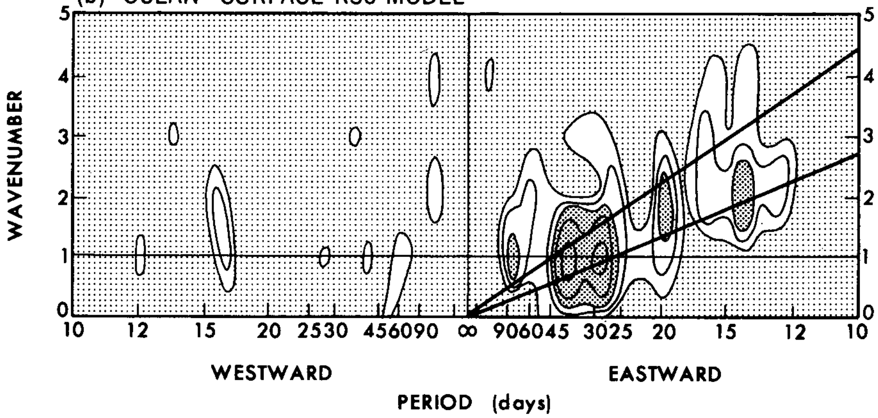

FIG. 17. As in Fig. 16 except for 830 mb. Contours 2, 5, 10, 20, 50, and 100 ($m^2 s^{-2}$ day). Dark shade > 20, light shade < 5.

and temperature probably results from adiabatic warming (or cooling) due to vertical motion outside the geographically localized heat source, as explained by Itoh and Nishi (1990).

Interestingly, the space–time spectra of the geopotential height of the ocean surface model (Fig. 19b) reveal eastward- and westward-moving 40–50- and 25–30-day peaks for the wavenumber-zero component as well, being contrary to the linear Kelvin mode, which is associated with a zero frequency for wavenumber zero. These wavenumber-zero oscillations correspond to the observed intraseasonal oscillations of zonal-mean angular momentum (Langley et al. 1981; Anderson and Rosen 1983; Lau et al. 1989). Probably, the wavenumber-zero oscillations result primarily from the wavenumber-one components through nonlinear effects such as conditional heating.

Goswami and Shukla (1984) found 20–40-day zonal velocity oscillations in a two-dimensional zonally symmetric general circulation model. Since these oscillations occur in the absence of a wavenumber-one component, they might be due to zonally symmetric low-frequency oscillations (Anderson and Stevens 1987) in the presence of basic Hadley (meridional–vertical) circulations or nonlinear symmetric instability (Zhao and Ghil 1991).

In the absence of Hadley circulations, the equatorial zonally symmetric component of a linear model on an equatorial beta plane has either zero frequency due to Kelvin and Rossby modes or high frequencies due to inertial gravity waves (Matsuno 1966). High-frequency inertial gravity waves can erroneously create low-frequency oscillations if the beta-plane equations are solved by use of the WKB approximation (Keshavamurti et al. 1986). This approximation is not always valid near the equator where the Coriolis parameter varies rapidly with latitude.

The preceding results demonstrate that both the 40–50- and 25–30-day oscillations can be simulated by an ocean-surface model with convective adjustment. The

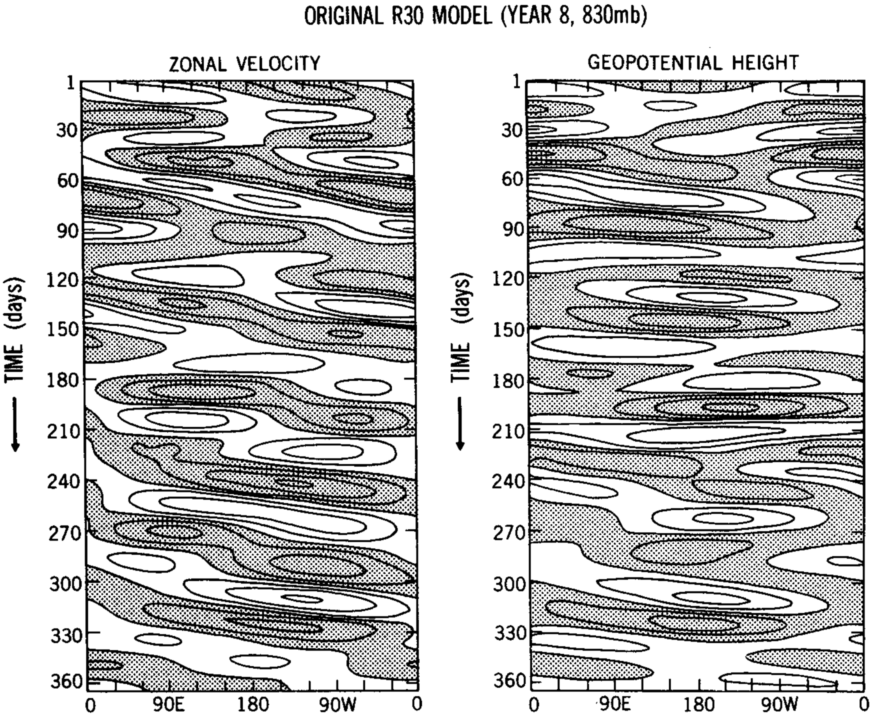

FIG. 18. Longitude–time sections of (a) the bandpass-filtered 830-mb zonal velocity and (b) the 830-mb geopotential height of the original R30 model (year 8). The filter is the sum of 40–50- and 25–30-day filters. Day 1 denotes 1 December of year 8. Contour intervals (a) 0.4 m $s^{-1}$, (b) 2.0 m. Dark shade indicates positive values.

absence of 40–50-day oscillations in the Tokyo University ocean-surface "aqua-planet" model, which has a horizontal resolution comparable to the R30 model, is probably due to the use of the Kuo-type parameterization (Kuo 1965) of convective heating.

Recently, Numaguti and Hayashi (1991a,b) compared aqua-planet models using the two parameterization schemes. Longitude–time sections of precipitation over a 90-day period indicate that the phase speed is more irregular with convective adjustment than when using the Kuo-type parameterization. This irregularity probably results from the presence of both 40–50- and 25–30-day oscillations that interfere with each other.

The present results suggest that the absence of 40–50-day oscillations in R15 ocean-surface models (Neelin et al. 1987; Lau et al. 1988) with convective adjustment is due to the low horizontal resolution. The absence of the 40–50-day mode in a low-resolution ocean-surface model with the modified Arakawa–Schubert-type parameterization (Tokioka et al. 1988) could be due to the parameterization scheme as well as the resolution.

### *b. Supercluster-scale oscillations*

Observed planetary-scale intraseasonal oscillations are accompanied by supercluster-scale oscillations with a half-wavelength of 2000–4000 km (Nakazawa 1988, Fig. 5), which corresponds to wavenumbers 5–10. It will be of interest here to examine the space–time spectra over a wider wavenumber–frequency range.

Figure 20 shows the wavenumber–frequency distributions of the space–time power spectra of (a) the 205-mb zonal velocity and (b) 205-mb geopotential height of the ocean surface model over the range of wavenumbers 0–10 and period domain of 2 days westward to 2 days eastward. In these figures, the major wavenumber-one 40–50- and 25–30-day peaks are not distinctly resolved due to the use of low-resolution spectra to obtain smoothed high-frequency spectra. These peaks are accompanied by high wavenumber-frequency minor peaks that appear along the two Kelvin wave dispersion lines passing through the points of the major peaks (45- and 27-day eastward-moving periods).

The geopotential spectra (Fig. 20b) indicate another wavenumber-one peak around an eastward-moving period of 10 days. This peak is accompanied by high wavenumber–frequency minor peaks along the 45 m $s^{-1}$ Kelvin-wave dispersion line that passes through wavenumber one at a period of 10 days. These peaks were also found at 100 mb (not illustrated) and correspond to the stratospheric 10–20-day Kelvin waves simulated by a previous ocean-surface model (Hayashi

POWER SPECTRA ($\phi$), 830mb, 10°N-10°S

(a) ORIGINAL R30 MODEL

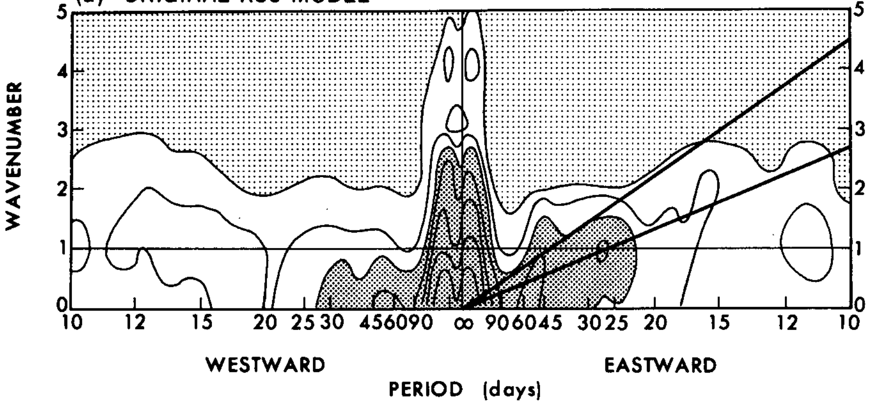

(b) OCEAN-SURFACE R30 MODEL

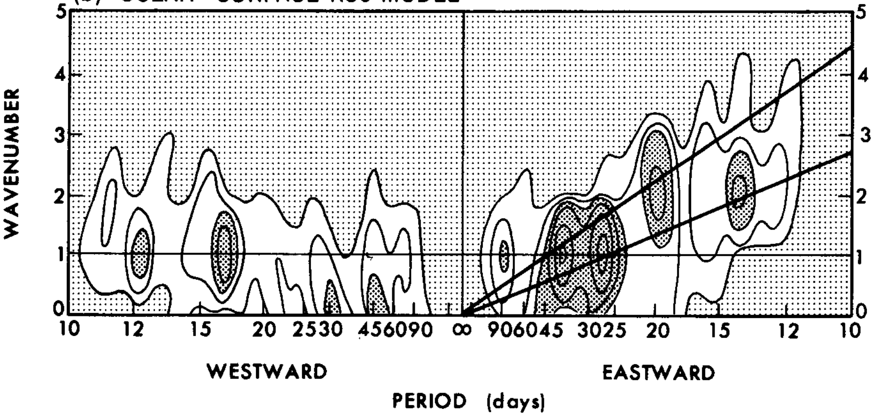

FIG. 19. As in Fig. 17 except for 830-mb geopotential height. Contours 2, 5, 10, 20, 50, 100, and 200 (10.0 $m^2$ day). Dark shade > 10, light shade < 2.

and Golder 1978). The minor peaks cannot be detected in the zonal velocity spectra (Fig. 20a). This is because the short-period zonal velocity spectra are suppressed, owing to the Kelvin wave zonal velocity being proportional to the period as well as geopotential height for a constant wavenumber [see Eq. (A7) in the Appendix]. The original model results also indicate (not illustrated) similar findings except that the peak appears as a 15-day peak, being in agreement with the SKYHI model (Fig. 13).

Figure 21 is the same as Fig. 20 except for (a) precipitation and (b) evaporation. The precipitation spectra resemble the vertical velocity spectra (not illustrated), being consistent with wave-CISK theory. These spectra exhibit wavenumber 5–10 components, which correspond to superclusters, in a much clearer manner than the zonal velocity spectra. This is due to Kelvin wave divergence being proportional to the wavenumber as well as the zonal velocity [see Eq. (A6)]. The wavenumber 5–10 components exhibit a large deviation from the two Kelvin wave dispersion lines toward higher wavenumbers and slower phase speeds. This deviation is in agreement with the observed OLR space–time spectra of Nakazawa (1986, Fig. 3). The wide range of wavenumbers indicates that superclusters are associated with a wider range of phase speeds than the planetary-scale oscillations.

Figure 21a also reveals a minor wavenumber-one 10–20-day precipitation peak, consistent with wave-CISK theory (Hayashi 1970) but contrary to random thermal-forcing theory (Holton 1973). The accompanying minor high wavenumber–frequency peaks along the Kelvin-wave dispersion line, which were found in the 200-mb geopotential height spectra, are not clearly defined owing to noise (the contours are not drawn). Probably, this results from short-period precipitation spectra being suppressed, since the Kelvin wave divergence is proportional to the period as well as geopotential height for a constant zonal wavenumber [see Eq. (A2)].

POWER SPECTRA, OCEAN-SURFACE MODEL, 10°N-10°S

(a) ZONAL VELOCITY (205mb)

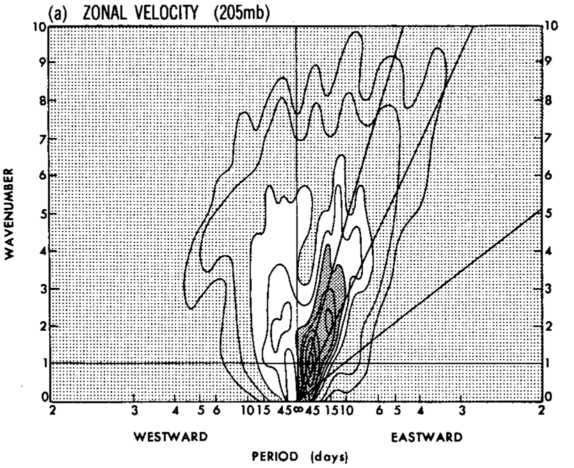

(b) GEOPOTENTIAL HEIGHT (205mb)

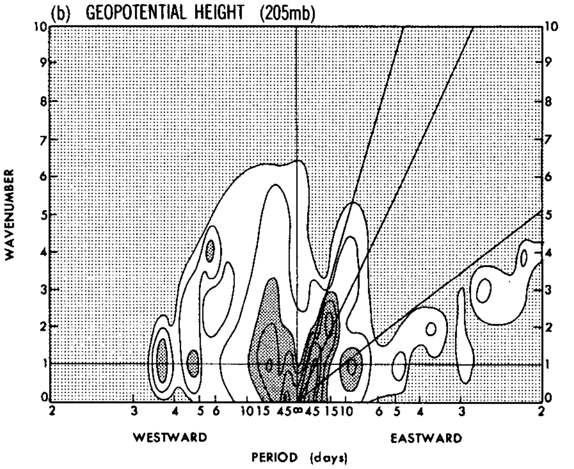

FIG. 20. Wavenumber-frequency distribution (ocean surface R30 model) of the space-time spectral density of the (a) 205-mb zonal velocity and (b) geopotential height averaged between 10°N and 10°S for the range of wavenumbers 0–10 and periods from 2 days westward to 2 days eastward. Slanted lines indicate Kelvin wave dispersion relations corresponding to eastward phase velocities of 10, 17, and 45 m $s^{-1}$ (see text). Contours (a) 5, 10, 20, 50, 100, 200, and 500 ($m^2 s^{-2}$ day); Dark shade > 20, light shade < 5. Contours (b) 1, 2, 5, 10, 20, 50, and 100 (10.0 $m^2$ day); Dark shade > 10, light shade < 2.

In contrast to the precipitation spectra, the evaporation spectra (Fig. 21b) are relatively concentrated in the planetary scale and resemble the surface zonal-velocity spectra (not illustrated), being consistent with the evaporation–wind feedback theory. This spectral distribution is also consistent with the experiments of Neelin et al. (1987), Lau et al. (1988), and Numaguti and Hayashi (1991a,b). These experiments demonstrated that, when the evaporation–wind feedback was removed from ocean-surface models, planetary-scale oscillations were greatly reduced while supercluster-scale oscillations were not appreciably affected.

### *c. Relationship between precipitation and vertical velocity*

Conditional heating plays a crucial role in wave-CISK and evaporation-wind feedback theories. It is, therefore, of importance to examine the relationship between precipitation and vertical velocity.

Figure 22 shows the longitudinal distributions on day 31 of the daily precipitation (upper panel) and 830-mb vertical pressure velocity (lower panel) along the equator of the ocean-surface model for wavenumber 0–30 (thin lines) and 0–1 (thick lines) components. Supercluster-scale waves can be seen in the wavenumber 0–30 components, while planetary-scale waves are represented by the wavenumber 0–1 component. For both scales, precipitation is mostly associated with upward motion, being consistent with conditional heating.

POWER SPECTRA, OCEAN-SURFACE MODEL, 10°N-10°S

(a) PRECIPITATION

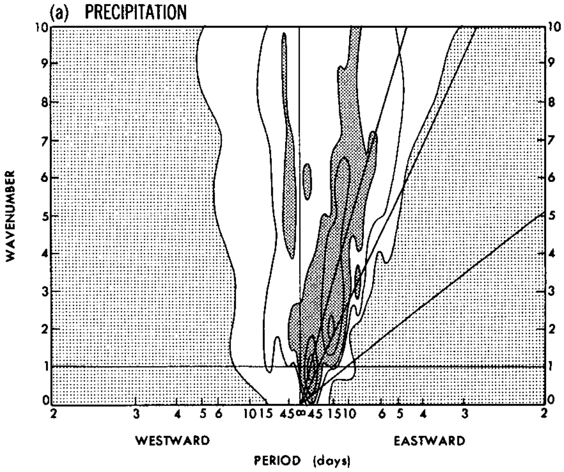

(b) EVAPORATION

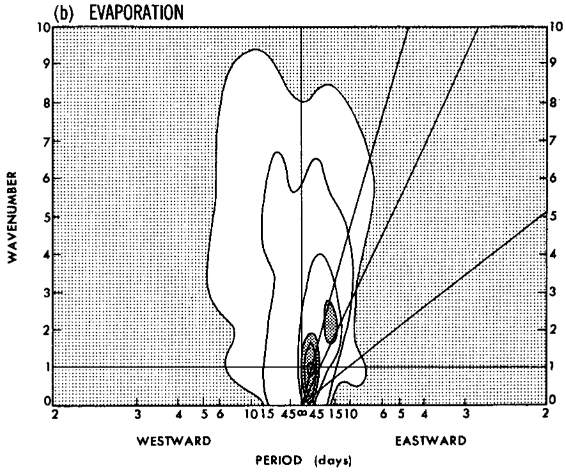

FIG. 21. As in Fig. 20 except for (a) precipitational heating and (b) evaporational cooling. Contours (a) 2, 5, 10, 20, and 50 (234.0 W2 $m^{-4}$ day); Dark shade > 10, light shade < 2. Contours (b) 1, 2, 5, 10, 20, and 50 (23.4 W2 $m^{-4}$ day); Dark shade > 10, light shade < 1.

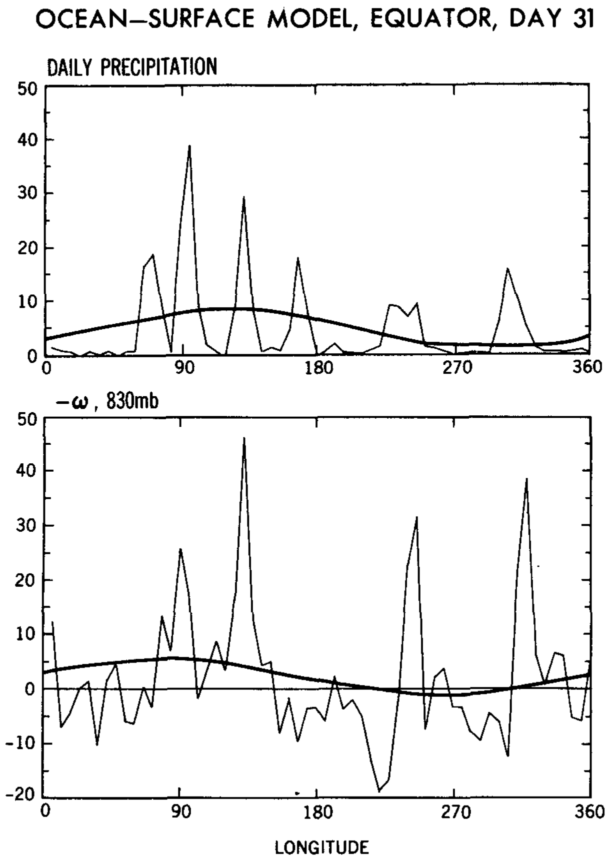

FIG. 22. Longitude distribution of (a) daily precipitational heating and (b) 830-mb vertical pressure velocity of the ocean surface R30 model (day 31, year 2) at the equator. Thin and thick lines indicate wavenumber 0–30 and 0–1 components, respectively. The units are (a) 48.4 W $m^{-2}$ and (b) $10^{-10}$ Pa $s^{-1}$.

In contrast to the Kuo-type parameterization, the model's convective adjustment scheme does not explicitly assume that precipitation occurs only with upward motion. However, this relationship probably results from convective heating being determined not just by the vertical gradient of temperature but also by humidity, which depends on moisture convergence and evaporation.

The planetary-scale equatorial vertical velocity of the ocean-surface model on other days and latitudes 10°N–10°S (not illustrated) is almost always upward due to the zonal-mean Hadley cell. Precipitation can also occur with weak downward motion when the loss of moisture due to low-level divergence is replenished by evaporation.

Figure 23 shows the time distributions of the precipitation (upper panel) and 830-mb vertical pressure velocity (lower panel) at 180° longitude at the equator of the original model. As can be seen, the precipitation is almost always associated with upward motion. The upward velocity is much greater than the downward velocity, being in agreement with those observed (not illustrated).

Planetary-scale oscillations can be isolated from supercluster-scale oscillations by taking an 11-day running mean. The running-mean equatorial vertical velocity (thick line) is almost always upward due to the local Hadley cell, in agreement with that observed (not illustrated). This conclusion holds for latitudes 10°N–10°S. This result suggests that an approximate linear relationship holds between planetary-scale intraseasonal vertical velocity and the precipitation fields, although these fields are nonlinearly affected by small-scale fields through conditional heating.

The original model results indicate (not illustrated) that evaporation exhibits a good correspondence with the surface velocity, which is almost always easterly at 180°. This justifies the linearization of the evaporation–wind relationship around the basic easterly flow in the linear evaporation–wind feedback theory (Neelin et al.

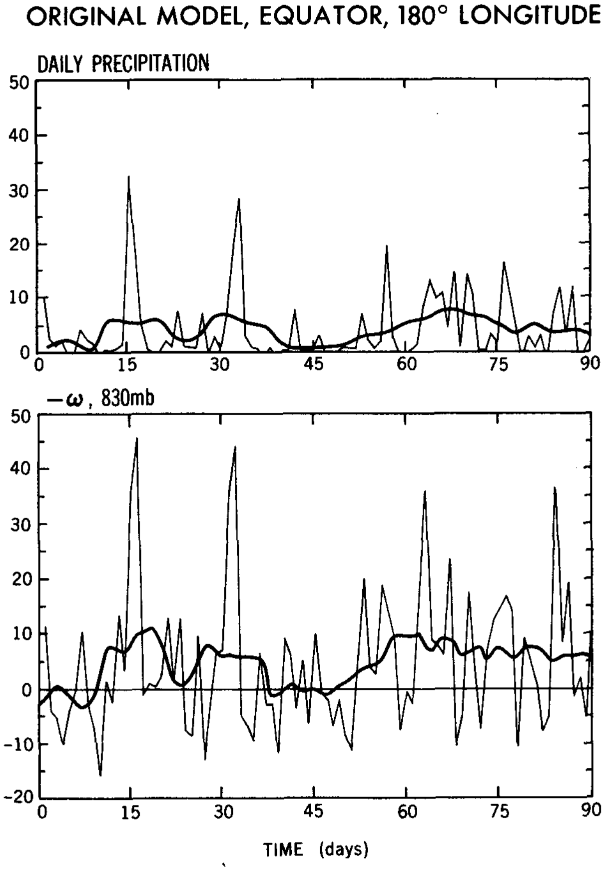

FIG. 23. Time distribution over 90 days of daily precipitational heating (a) and 830-mb vertical pressure velocity of the original R30 model (year 8) at 180° longitude. Day 1 denotes 1 December. Thin and thick lines indicate daily and 11-day running mean values, respectively. The units are (a) 48.4 W $m^{-2}$ and (b) $10^{-10}$ Pa $s^{-1}$.

1987; Emanuel 1987). On the other hand, the ocean surface model indicates (not illustrated) that the surface zonal velocity has a weak basic easterly flow and oscillates between easterly and westerly, as in the nonlinear evaporation–wind feedback theory (Xie 1991). The planetary-scale zonal velocity field is almost always easterly, however.

### *d. Propagation of planetary- and supercluster-scale oscillations*

According to thermal-forcing theories, a global eastward propagation of winds can occur even if the amplitude of the eastward-propagating heat oscillation is geographically localized. It is of interest here to compare the propagation of precipitation simulated by the two R30 models.

Figure 24 shows the longitude–time distributions of daily precipitation along the equator of the (a) original and (b) ocean-surface models. The original model results indicate that precipitation is concentrated in several longitudinal belts with some degree of eastward phase propagation, in agreement with observed outgoing longwave radiation (e.g., Nakazawa 1988; Lau and Chan 1985, 1986a; Knutson et al. 1986; Knutson and Weichmann 1987). The ocean-surface model more clearly reveals the eastward propagation, which is mainly due to supercluster-scale oscillations and is partly due to planetary-scale oscillations.

Figure 25 compares the longitude–time distribution of the original model's daily precipitation along the equator during the period May through August (year 8) with that of the observed 1980 OLR; observed precipitation is not included in the ECMWF dataset. It can be seen that both the precipitation and OLR exhibit eastward phase propagation, having larger amplitudes over the Pacific than over the Atlantic.

To isolate planetary-scale oscillations from supercluster-scale oscillations, Fig. 26 displays the longitude–time distributions of the sum of 40–50- and 25–30-day filtered precipitation oscillations of (a) the original model and (b) the ocean surface model. Similar results were obtained when the 40–50- and 25–30-day filters were applied separately (not illustrated).

In the original model (Fig. 26a), the amplitudes of these oscillations are localized in several longitude belts; major and minor amplitudes occur over the Pacific and Atlantic, respectively. The localized eastward phase

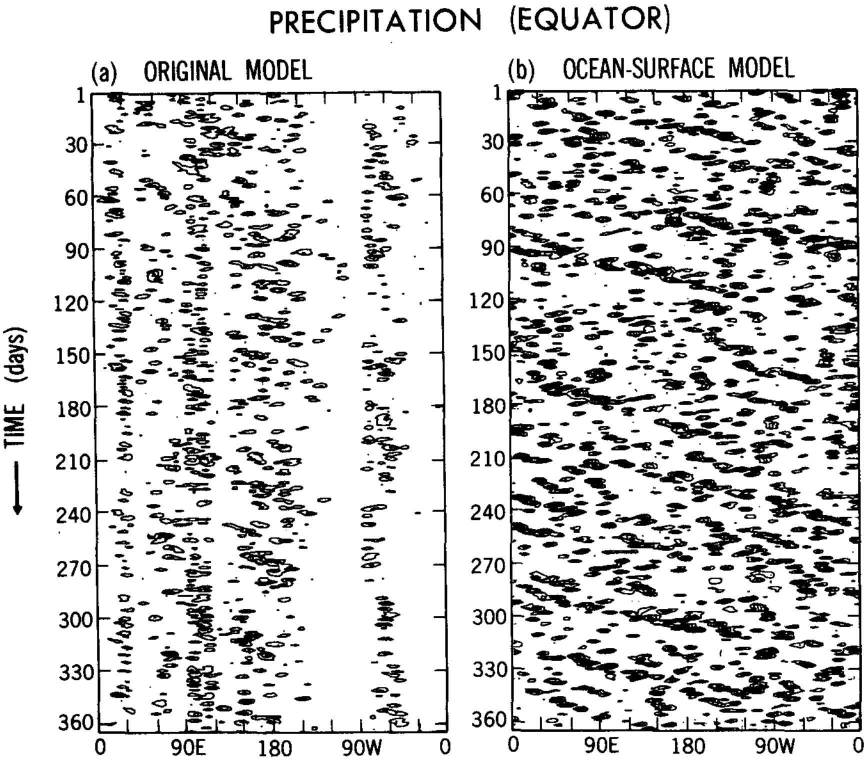

FIG. 24. Longitude–time distribution of daily precipitational heating at the equator of (a) the original R30 model and (b) the ocean surface R30 model. The seasonal variation has been subtracted from the original model precipitation. Day 1 denotes (a) 1 December of year 8 and (b) the first day of year 2. Contours are drawn for positive values only. Contour values are (a) 5, 20, 35, 50, and 65 (48.4 W m$^{-2}$) and (b) 6, 12, 18, 24, 30, 36, 42, 48, 54, 60, and 66 (48.4 W m$^{-2}$).

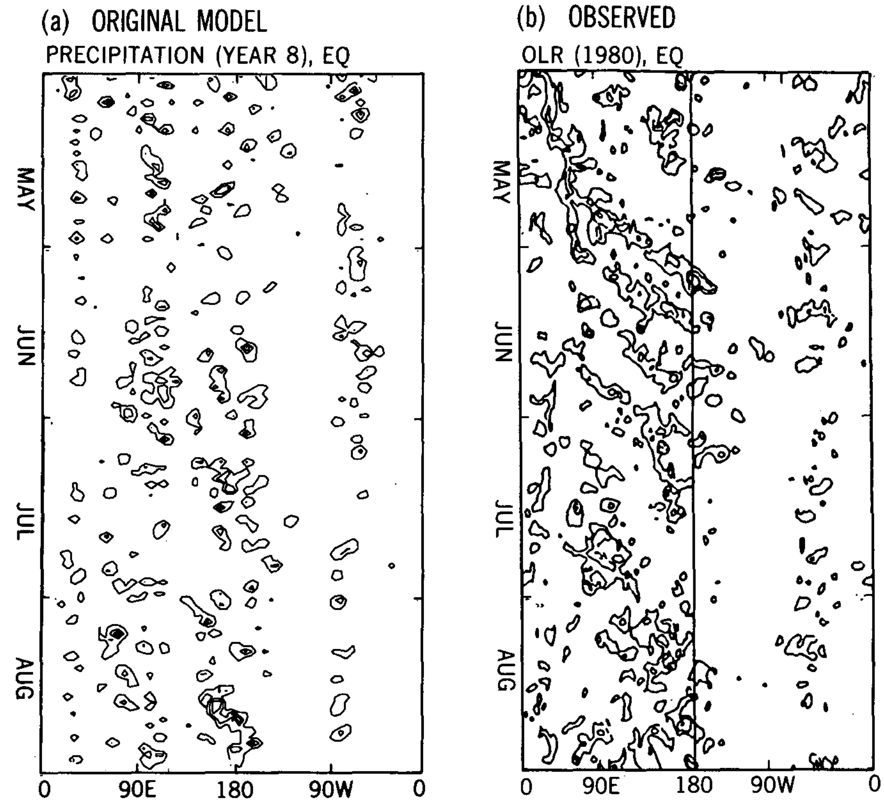

FIG. 25. Longitude–time distribution (May–August, equator) of (a) the daily precipitational heating of the original R30 model and (b) the observed outgoing longwave radiation for the year 1980 (after Hayashi and Nakazawa 1989). The seasonal variation was subtracted. Contours are drawn for (a) positive and (b) negative values only. Contour values are (a) 5, 20, 35, 50, and 65 (48.4 W $m^{-2}$) and (b) −20, −60, and −100 (W $m^{-2}$).

speeds are slower than the global phase speed of the eastward propagation between the major and minor maxima.

The global eastward propagation of the intraseasonal precipitation oscillation is more clearly seen in the ocean-surface model (Fig. 26b). Here, the 40–50- and 25–30-day oscillations are associated with not only the planetary scale but also smaller scales. The higher-wavenumber components are not concentrated in certain longitudinal belts and randomly migrate in both eastward and westward directions.

The foregoing analysis suggests that the sea surface temperature geographically modulates the intrinsically eastward-moving wavenumber-one precipitation oscillations, resulting in their major Pacific and minor Atlantic maxima along with a slow local phase speed. This in turn results in the global phase propagation of the zonal velocity with weak nodes and the standing oscillation of geopotential height with strong nodes. This interpretation is more in line with the results of the model having a nearly confined heat propagation (Hayashi and Miyahara 1987) than the results of thermal-forcing models with a strictly confined heat pulsation (Yamagata and Hayashi 1984) and a strictly confined heat propagation (Itoh and Nishi 1990).

## 8. Conclusions and remarks

To clarify differences between tropical 40–50- and 25–30-day oscillations and to evaluate both simulations and theories, space–time spectrum and filter analyses have been conducted over nine years of data from a nine-level, 30-wavenumber (R30) spectral GCM having climatological-mean sea surface temperatures. Similar analyses were performed on the ECMWF four-dimensional analysis dataset over nine years (1979–87), which includes the FGGE year of 1979. In addition, the effects of increased vertical resolution were examined by integrating the 40-level, three-degree grid (N30) GFDL SKYHI model over three years. The effects of the absence of geography and seasonal variations were examined by integrating an ocean-surface perpetual January R30 model over three years. The following conclusions were obtained.

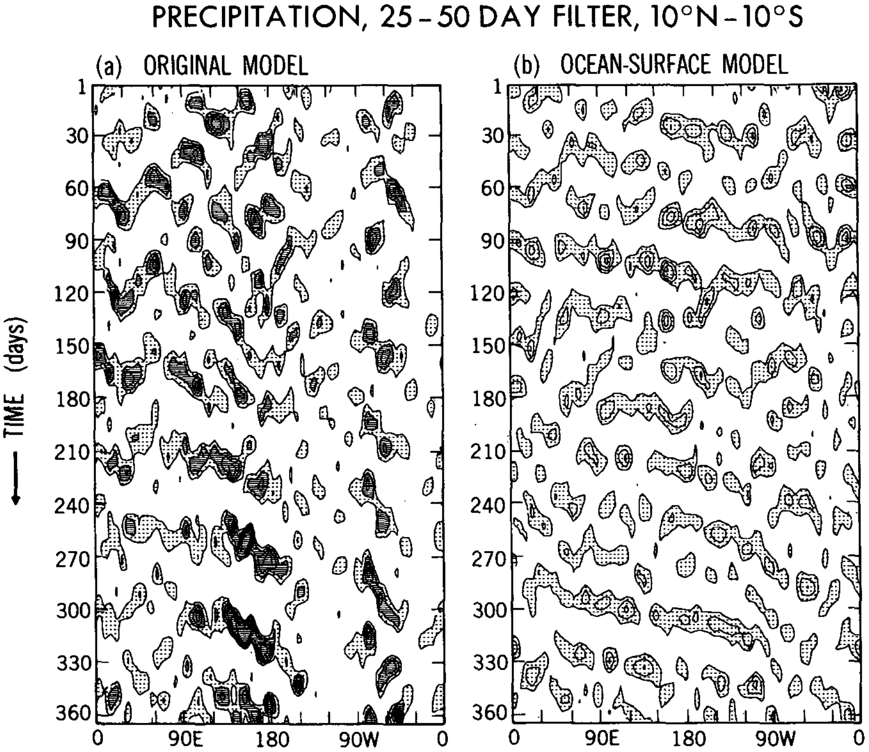

FIG. 26. As in Fig. 24 except for the sum of 40–50- and 25–30-day filtered precipitational heating averaged over 10°N–10°S. Contours are drawn for positive values only. Contour values are (a) 2, 6, 10, 14, and 18 (4.84 W $m^{-2}$) and (b) 3, 9, 15, and 21 (4.84 W $m^{-2}$).

1) The space–time spectra of the simulated zonal velocity exhibit 40–50- and 25–30-day period peaks for the wavenumber-one eastward-moving component, having comparable magnitudes in the nine-year average. These two peaks can be identified in most of the individual-year spectra, with one peak dominating the other for several of the years. The corresponding observed spectra indicate an eastward-moving wavenumber-one peak at 50–60 days. A minor eastward-moving 25–30-day peak can also be detected in several observed individual-year spectra, although it is obscured in the nine-year average.

2) The nine-year average variance of the simulated 40–50-day oscillations is in agreement with that of the observed 50–60-day oscillations, while the average variance of the simulated 25–30-day oscillations is much stronger than that observed. This conclusion differs from the previous results of Hayashi and Golder (1986, 1988); namely, that the simulated 40–50 day variance is too weak, while the simulated 25–30-day variance is comparable to that observed in the FGGE year.

3) The simulated 40–50- and 25–30-day zonal velocity oscillations have similar longitudinal distributions of time variance, implying that the two periods are not due to different local phase speeds that depend on the local time-mean flow through linear advection. They grow and decay independently, indicating that the two periods are not due to the seasonal modulation of an intrinsic 30–40-day period.

4) The model exhibits an eastward-moving Kelvin-mode pattern in the upper equatorial troposphere and an eastward-moving Rossby-mode pattern away from the equator, consistent with a thermal-forcing model. In contrast, the observed zonal velocity does not exhibit a maximum amplitude over the equator and is, particularly in the non-FGGE years, more than 90 degrees out of phase with geopotential height, contrary to the Kelvin mode. These distortions can be due to nonlinear advection or vertical momentum transport by transient gravity waves and cumulus convection that is not parameterized in the model.

5) The R30 model and the observed data indicate that the 40–50- and 25–30-day oscillations have similar horizontal and vertical structures. The 25–30-day oscillations exhibit a slightly greater increase with height in their tropospheric amplitudes of zonal velocity and convective heating than 40–50-day oscillations, however, resulting in different relative magnitudes at different levels. For both oscillations, the temperature is

nearly in phase with the vertical velocity in the middle troposphere, implying the conversion of eddy potential energy into eddy kinetic energy. Also, the vertical velocity and convective heating are nearly in phase, both tilting westward with height in the lower troposphere.

6) The results of the 40-level SKYHI model indicate that the 25–30-day oscillations still appear too strong. Nevertheless, this model reveals a longer vertical wavelength and a higher penetration of amplitude above the level of tropospheric convective heating for the 25-day oscillations than the 40–50-day oscillations. The stratospheric 10–20-day oscillations have a longer vertical wavelength than the 25–30-day oscillations. This suggests that the three oscillations differ in their intrinsic vertical wavelengths. The SKYHI model reveals a slight increase in the height of maximum convective heating amplitude with periods. The maxima for all three oscillations occur in the middle troposphere, however, contrary to the most unstable vertical mode of the wave–CISK theory.

7) The results of the ocean-surface perpetual January R30 model indicate that both the wavenumber-one 40–50- and 25–30-day peaks occur, even in the absence of geographical and seasonal variations. Both the realistic and idealized R30 models reveal higher wavenumber–frequency peaks in precipitation, corresponding to the eastward propagation of supercluster-scale (wavenumber 5–10) oscillations. These models also show that precipitation occurs mostly with upward motion, consistent with conditional heating. The planetary-scale vertical velocity field is almost always upward due to the zonal-mean Hadley cell, however, justifying the linear relationship among planetary-scale variables.

8) A comparison between the two R30 models suggests that the sea surface temperature geographically modulates the intrinsically wavenumber-one eastward-propagating precipitation oscillations, resulting in their major Pacific and minor Atlantic local amplitudes. This in turn causes eastward-moving zonal-velocity oscillations and standing geopotential oscillations, consistent with a thermal-forcing theory having nearly confined propagating heating.

This study is the first to show that the R30 model produces 40–50-day oscillations that are comparable, in the nine-year average amplitude, to those observed. The R30 model tends to produce 25–30-day oscillations that are on the average too strong, however, while the R15 model does not exhibit 40–50-day oscillations. There remains some possibility that air–sea interactions might reduce 25–30-day oscillations more effectively than 40–50-day oscillations.

It is also possible that when the horizontal resolution is drastically increased, the 40–50-day oscillation might even become too strong due to increased frictional meridional convergence, which is more efficient for low-frequency oscillations than high-frequency oscillations (Hayashi 1971a,b). On the other hand, owing to an increased transient wave drag, the amplitudes of both oscillations might become more realistic and the Kelvin wave patterns more distorted than those observed. Kanamitsu et al. (1972) found that low-wavenumber waves lose kinetic energy to high-wavenumber waves in the tropics, while Sheng and Hayashi (1990) showed that low-frequency oscillations lose energy to high-frequency oscillations. Hayashi et al. (1989) demonstrated that the gravity-wave momentum flux in the SKYHI model increases with horizontal resolution, resulting in weaker and more realistic stratospheric and mesospheric zonal flows.

Another possibility is that improvements in the convective parameterization schemes might result in stronger 40–50-day oscillations. The present model with the Manabe-type parameterization (moist convective adjustment) simulates both 40–50- and 25–30-day oscillations. The Kuo-type parameterization results in only 20–40-day oscillations (Hayashi and Sumi 1986), while the Arakawa–Schubert-type parameterization (Arakawa and Schubert 1974) produces 10–20-day oscillations (Tokioka et al. 1988).

The Arakawa–Shubert parameterization can be modified in such a way that the convective heating maximum will occur in the middle troposphere instead of the upper troposphere, resulting in 20–40-day oscillations (Tokioka et al. 1988). However, if the convective heating due to the Manabe-type parameterization were unrealistically confined to the lower troposphere, the 40–50- and 25–30-day peaks would probably appear as 80–100- and 40–50-day peaks, respectively.

Similarly, if the convective heating due to the Kuo and Arakawa–Schubert parameterizations were confined to the lower troposphere, the 20–40-day peak would probably shift to a 40–50-day peak. Swinbank et al. (1988) found a similar shift in an ocean surface model with a doubled latent heat constant, while Kuma (1990b) found a similar shift in a realistic model with doubled longwave radiation that resulted in increased Kuo-type convective heating in the lower troposphere. The present study suggests, however, that parameterization and radiation schemes should be improved, if necessary, so that the 25–30-day peak appears weaker than the 40–50-day peak, instead of the 25–30-day peak shifting to the 40–50-day peak.

The space–time spectral analysis of two low-resolution general circulation models (Park et al. 1990, Fig. 6), each integrated over two years, revealed a weak 40–50-day peak in both models and a strong 25–30-day peak in one model. These models have the same parameterization but different finite-difference schemes. Both models indicate that the convective heating amplitudes associated with the dominant periods are strongest in the middle troposphere but have slightly different vertical distributions in the lower troposphere, as was also found in the present R30 and SKYHI models. This difference does not imply, however, that the dominant period is highly sensitive to the vertical distribution, since the dominant period is due to the relative magnitudes of the two spectral peaks. If the two low-resolution models were integrated long enough, each model would probably indicate weak 40–50- and strong 25–30-day peaks in the long-term average, with the relative magnitudes varying from year to year.

This study is also the first to demonstrate that both the 40–50- and 25–30-day oscillations are simulated in an ocean-surface perpetual January model. This finding suggests that a theoretical model should be able to simulate not only the 25–30-day but also the 40–50-day oscillations in the absence of topography and seasonal variations.

The tilt of the vertical velocity oscillations in the lower troposphere is probably due to frictional convergence. This tilt is associated with an in-phase relationship between the low-level vertical velocity and the surface wind. This in-phase relationship implies an in-phase relationship between surface convergence and evaporation. Thus, wave-CISK and evaporation–wind feedback should act conjointly in the presence of frictional convergence. Future evaporation–wind feedback models should include an adequate boundary layer to reproduce these relationships.

The present analysis revealed a phase lag between the low-level vertical velocity and upper-level convective heating. It is difficult, however, to interpret this lag as justification for the phase-lagged wave-CISK parameterization of Davis (1979), since this theory included neither surface friction nor the vertical tilt of heating. The vertical tilt of convective heating should also be incorporated in future wave-CISK and evaporation–wind feedback models.

The most serious defect of the current wave-CISK and evaporation–wind feedback theories is that neither explains the observed and simulated 40–50-day periodicity, even if the governing equations are fully nonlinear. An improved or new theory should be able to explain not only the 25–30-day oscillations but also the 40–50- and 10–20-day oscillations, and the supercluster-scale oscillations.

The equatorial (10°N–10°S) planetary-scale vertical velocity is found to be almost always upward, implying that an approximate linear relationship will hold between planetary-scale vertical velocity and conditional heating. Although planetary-scale oscillations are nonlinearly affected by small-scale oscillations through conditional heating, this finding justifies the interpretation of the structure and propagation of planetary-scale intraseasonal oscillations in terms of linear theories. The similarities and differences in structure between the 40–50- and 25–30-day oscillations should be studied by both linear and nonlinear thermal-forcing models. The nonlinear effect might explain the observed distortion of the Kelvin wave pattern, particularly when the forcing is localized.

For better model–observation comparisons of intraseasonal oscillations, a future reanalysis dataset (see Kinter and Shukla 1989; Kalnay and Jenne 1991) should have more vertical resolution than the present ECMWF data. The distortion found in the observed Kelvin-wave patterns could be partly due to possible inaccuracies in wind and geopotential height data. Also, observational estimates of the vertical distribution of convective heating are of crucial importance to evaluate the various convective parameterization schemes.

*Acknowledgments.* The authors are grateful to Dr. S. Manabe for his advice and to Drs. N.-C. Lau, I. M. Held, J. D. Mahlman, and Mr. T. R. Knutson for their comments on the original manuscript. Suggestions from two anonymous reviewers led to significant improvements in the revised manuscript. Thanks are extended to Mr. P. Tunison for the drafting of the figures.

## APPENDIX

### Relationship between Kelvin Wave Variables

Since a Kelvin mode has no meridional component, the linearized zonal momentum and continuity equations in the absence of a basic flow are reduced to

$$\partial u/\partial t = -\partial\phi/\partial x, \tag{A1}$$

$$\partial u/\partial x = -\partial\omega/\partial p, \tag{A2}$$

where $u$, $\phi$, and $\omega$ are the zonal velocity, geopotential, and vertical pressure velocity, respectively.

For a zonally propagating wave of the form

$$\exp(ikx + i\sigma t), \tag{A3}$$

where $k$ and $\sigma$ are the zonal wavenumber and angular frequency, respectively, Eqs. (A1) and (A2) are reduced to

$$i\sigma u = -ik\phi, \tag{A4}$$

$$iku = -\partial\omega/\partial p. \tag{A5}$$

It follows from Eqs. (A4) and (A5) that the zonal velocity, geopotential, and divergence are related as

$$\phi = -\frac{\sigma}{k}u = cu, \tag{A6}$$

$$u = \frac{i}{k}\frac{\partial\omega}{\partial p}, \tag{A7}$$

$$\phi = -\frac{i\sigma}{k^2}\frac{\partial\omega}{\partial p} = \frac{ic}{k}\frac{\partial\omega}{\partial p}, \tag{A8}$$

where the phase speed $c$ is given by

$$c = -\frac{\sigma}{k}. \qquad \text{(A9)}$$

In the presence of a basic flow $U$, the phase speed and frequency are replaced by the relative phase speed $(c - U)$ and intrinsic frequency $(\sigma + kU)$, respectively.

## REFERENCES

Anderson, J. R., and R. D. Rosen, 1983: The latitude-height structure of 40–50-day variations in atmospheric angular momentum. *J. Atmos. Sci.*, **40**, 1584–1591.

——, and D. E. Stevens, 1987: The presence of linear wavelike modes in a zonally symmetric model of the tropical atmosphere. *J. Atmos. Sci.*, **44**, 2115–2127.

Arakawa, A., and W. H. Schubert, 1974: Interaction of a cumulus cloud ensemble with the large-scale environment. Part I. *J. Atmos. Sci.*, **31**, 674–701.

Bengtsson, L., M. Kanamitsu, P. Kallberg, and S. Uppals, 1982: FGGE four-dimensional data assimilation at ECMWF. *Bull. Amer. Meteor. Soc.*, **63**, 29–43.

Chang, C.-P., 1976: Forcing of stratospheric Kelvin waves by tropospheric heat sources. *J. Atmos. Sci.*, **33**, 740–744.

——, 1977: Viscous internal gravity waves and low-frequency oscillations in the tropics. *J. Atmos. Sci.*, **34**, 901–910.

——, and H. Lim, 1988: Kelvin wave–CISK: A possible mechanism for the 30–50-day oscillations? *J. Atmos. Sci.*, **45**, 1709–1720.

Chao, W. C., 1987: On the origin of the tropical intraseasonal oscillation. *J. Atmos. Sci.*, **44**, 1940–1949.

Chen, T.-C., 1985: On the time variation in the tropical energetics of large-scale motions during the FGGE summer. *Tellus*, **37A**, 258–275.

Crum, F. X., and T. J. Dunkerton, 1992: Analytic and numerical models of wave-CISK with conditional heating. *J. Atmos. Sci.*, **49**, 1693–1708.

Davey, M. K., 1989: A simple tropical moist model applied to the "40-day" wave. *Quart. J. Roy. Meteor. Soc.*, **115**, 1071–1107.

Davis, H. C., 1979: Phase-lagged wave-CISK. *Quart. J. Roy. Meteor. Soc.*, **105**, 323–353.

Dunkerton, T. J., and F. X. Crum, 1991: Scale-selection and propagation of wave–CISK with conditional heating. *J. Meteor. Soc. Japan*, **69**, 449–458.

Emanuel, K. A., 1987: An air–sea interaction model of intraseasonal oscillations in the tropics. *J. Atmos. Sci.*, **44**, 2324–2340.

Garcia, R. R., and M. L. Salby, 1987: Transient response to localized episodic heating in the tropics. Part II: Far-field behavior. *J. Atmos. Sci.*, **44**, 499–530.

Gill, A. E., 1980: Some simple solutions for heat-induced tropical circulation. *Quart. J. Roy. Meteor. Soc.*, **106**, 447–462.

Gordon, C. T., and W. F. Stern, 1982: A description of the GFDL global spectral model. *Mon. Wea. Rev.*, **110**, 625–644.

Goswami, B. N., and J. Shukla, 1984: Quasi-periodic oscillations in a symmetric general circulation model. *J. Atmos. Sci.*, **41**, 20–37.

Gutzler, D. S., and R. D. Madden, 1989: Seasonal variations in the spatial structure of intraseasonal tropical wind fluctuations. *J. Atmos. Sci.*, **46**, 641–660.

Hayashi, Y., 1970: A theory of large-scale equatorial waves generated by condensational heat and accelerating the zonal wind. *J. Meteor. Soc. Japan*, **48**, 140–160.

——, 1971a: Frictional convergence due to large-scale equatorial waves in a finite-depth Ekman layer. *J. Meteor. Soc. Japan*, **49**, 450–457.

——, 1971b: Large-scale equatorial waves destabilized by convective heating in the presence of surface friction. *J. Meteor. Soc. Japan*, **49**, 458–466.

——, 1971c: Instability of large-scale equatorial waves under the radiation condition. *J. Meteor. Soc. Japan*, **49**, 316–319.

——, 1971d: Instability of large-scale equatorial waves with a frequency-dependent CISK parameter. *J. Meteor. Soc. Japan*, **49**, 59–62.

——, 1974: Spectral analysis of tropical disturbances appearing in a GFDL general circulation model. *J. Atmos. Sci.*, **31**, 180–218.

——, 1976: Non-singular resonance of equatorial waves under the radiation condition. *J. Atmos. Sci.*, **33**, 183–201.

——, 1982: Space-time spectral analysis and its applications to atmospheric waves. *J. Meteor. Soc. Japan*, **60**, 156–171.

——, and D. G. Golder, 1978: The generation of equatorial transient planetary waves: Control experiments with a GFDL general circulation model. *J. Atmos. Sci.*, **35**, 2068–2082.

——, and ——, 1980: The seasonal variation of tropical transient planetary waves appearing in a GFDL general circulation model. *J. Atmos. Sci.*, **37**, 705–716.

——, and ——, 1981: The effects of condensational heating on middle latitude transient waves in their mature stage: Control experiments with a GFDL general circulation model. *J. Atmos. Sci.*, **38**, 2532–2539.

——, and ——, 1986: Tropical intraseasonal oscillations appearing in a GFDL general circulation model and FGGE data, Part I: Phase propagation. *J. Atmos. Sci.*, **43**, 3058–3067.

——, and S. Miyahara, 1987: A three-dimensional linear response model of the tropical intraseasonal oscillation. *J. Meteor. Soc. Japan*, **65**, 843–857.

——, and D. G. Golder, 1988: Tropical intraseasonal oscillations appearing in a GFDL general circulation model and FGGE data. Part II: Structure. *J. Atmos. Sci.*, **45**, 3017–3033.

——, ——, and J. D. Mahlman, 1984: Stratospheric and mesospheric Kelvin waves simulated by the GFDL "SKYHI" general circulation model. *J. Atmos. Sci.*, **41**, 1971–1984.

——, ——, ——, and S. Miyahara, 1989: The effect of horizontal resolution on gravity waves simulated by the GFDL "SKYHI" general circulation model. *Pure Appl. Geophys.*, **130**, 421–443.

Hayashi, Y.-Y., and T. Nakazawa, 1989: Evidence of the existence and eastward motion of superclusters at the equator. *Mon. Wea. Rev.*, **117**, 236–243.

——, and A. Sumi, 1986: The 20–40-day oscillation simulated in an "aqua-planet" model. *J. Meteor. Soc. Japan*, **64**, 431–466.

Hendon, H. H., 1988: A simple model of the 40–50-day oscillation. *J. Atmos. Sci.*, **45**, 569–584.

Hirota, I., 1979: Kelvin waves in the equatorial middle atmosphere observed by the Nimbus 5 SCR. *J. Atmos. Sci.*, **36**, 217–222.

Hollingsworth, A., C. Lorenc, M. S. Tracton, K. Arpe, G. Cats, S. Uppala, and P. Kallberg, 1985: The response of numerical weather prediction systems to FGGE IIb data. Part I: Analyses. *Quart. J. Roy. Meteor. Soc.*, **111**, 1–66.

——, D. B. Shaw, P. Lonnberg, L. Illam, K. Arpe, and A. J. Simmons, 1986: Monitoring of observations and analysis quality by a data assimilation system. *Mon. Wea. Rev.*, **114**, 861–879.

Holton, J. R., 1973: On the frequency distribution of atmospheric Kelvin waves. *J. Atmos. Sci.*, **30**, 499–501.

Hsu, H.-H., B. J. Hoskins, and F. F. Jin, 1990: The 1985/86 intraseasonal oscillation and the role of the extratropics. *J. Atmos. Sci.*, **47**, 823–839.

Itoh, H., 1989: The mechanism for the scale selection of tropical intraseasonal oscillations: Part I: Selection of wavenumber 1 and the three-scale structure.. *J. Atmos. Sci.*, **46**, 1779–1798.

——, and N. Nishi, 1990: Consideration for the structure of the tropical intraseasonal oscillation. *J. Meteor. Soc. Japan*, **68**, 659–675.

Kalnay, E., and R. Jenne, 1991: Summary of the NMC/NCAR reanalysis workshop of April 1991. *Bull. Amer. Meteor. Soc.*, **72**, 1897–1904.

Kanamitsu, M., T. N. Krishnamurti, and C. Depradine, 1972: On scale interactions in the tropics during Northern Summer. *J. Atmos. Sci.*, **29**, 698–706.

Keshavamurti, R. N., S. V. Kasture, and V. Krishnakumar, 1986:

30–50-day oscillation of the Monsoon: A new theory. *Beitr. Phys. Atmos.*, **59**, 443–454.

Kinter, J. L., and J. Shukla, 1989: Reanalysis for TOGA (Tropical Oceans, Global Atmosphere). 1–3 February 1989 meeting at the Center for Ocean-Land-Atmosphere Interactions. *Bull. Amer. Meteor. Soc.*, **70**, 1422–1427.

Knutson, T. R., and K. M. Weickmann, 1987: 30–60-day atmospheric oscillations: Composite life cycles of convection and circulation anomalies. *Mon. Wea. Rev.*, **115**, 1407–1436.

——, ——, and J. E. Kutzbach, 1986: Global scale intraseasonal oscillations of outgoing longwave radiation and 250-mb zonal wind during Northern Hemisphere summer. *Mon. Wea. Rev.*, **114**, 605–623.

Krishnamurti, T. N., P. K. Jayakumar, J. Sheng, N. Surgi, and A. Kumar, 1985: Divergent circulation on the 30- to 50-day time scale. *J. Atmos. Sci.*, **42**, 364–375.

Kuma, K., 1990a: A quasi-biennial oscillation in the intensity of the intraseasonal oscillation. *Int. J. Climatol.*, **10**, 263–278.

——, 1990b: Diabatic heating and the low frequency dynamics in the tropics. *Meteor. Atmos. Phys.*, **44**, 265–279.

Kuo, H.-L., 1965: On formation and intensification of tropical cyclones through latent heat release by cumulus convection. *J. Atmos. Sci.*, **22**, 40–63.

——, 1975: Instability theory of large-scale disturbances in the tropics. *J. Atmos. Sci.*, **32**, 2229–2245.

Langley, R. G., R. W. King, I. I. Shapiro, R. D. Rosen, and D. A. Salstein, 1981: Atmospheric angular momentum and the length of day: A common fluctuation with a period near 50 days. *Nature*, **294**, 730–732.

Lau, K.-M., and P. H. Chan, 1985: Aspects of the 40–50-day oscillation during the northern winter as inferred from outgoing longwave radiation. *Mon. Wea. Rev.*, **113**, 1889–1909.

——, and ——, 1986a: Aspects of the 40–50 day oscillation during the northern summer as inferred from outgoing longwave radiation. *Mon. Wea. Rev.*, **114**, 1354–1367.

——, and ——, 1986b: The 40–50-day oscillations and the El Niño Southern Oscillation: A new perspective. *Bull. Amer. Meteor. Soc.*, **67**, 533–534.

——, and ——, 1988: Intraseasonal and interannual variations of tropical convection: A possible link between the 40–50-day oscillation and ENSO? *J. Atmos. Sci.*, **45**, 506–521.

——, and H. Lim, 1982: Thermally driven motions in an equatorial beta-plane: Hadley and Walker circulations during the winter monsoon. *Mon. Wea. Rev.*, **110**, 336–353.

——, and L. Peng, 1987: Origin of low frequency (intraseasonal) oscillations in the tropical atmosphere. Part I: Basic theory. *J. Atmos. Sci.*, **44**, 950–972.

——, I.-S. Kang, and P. J. Sheu, 1989: Principal modes of intraseasonal variations in atmospheric angular momentum and tropical convection. *J. Geophys. Res.*, **94**, 6319–6332.

Lau, N.-C., and K.-M. Lau, 1986: The structure and propagation of intraseasonal oscillations appearing in a GFDL GCM. *J. Atmos. Sci.*, **43**, 2023–2047.

——, I. M. Held, and J. D. Neelin, 1988: The Madden–Julian oscillation in an idealized general circulation model. *J. Atmos. Sci.*, **45**, 3810–3932.

Lim, H., T.-K. Lim, and C.-P. Chang, 1990: Reexamination of wave–CISK theory: Existence and properties of nonlinear wave-CISK modes. *J. Atmos. Sci.*, **47**, 3078–3091.

Lindzen, R. S., 1967: Planetary waves on beta planes. *Mon. Wea. Rev.*, **95**, 441–451.

——, 1974: Wave-CISK in the tropics. *J. Atmos. Sci.*, **31**, 156–179.

——, and T. Matsuno, 1968: On the nature of a large-scale wave disturbances in the equatorial stratosphere. *J. Meteor. Soc., Japan*, **46**, 215–221.

Lorenc, A. C., 1984: The evolution of planetary scale 200-mb divergent flow during the FGGE year. *Quart. J. Roy. Meteor. Soc.*, **110**, 427–441.

Madden, R. A., 1979: Observations of large-scale traveling Rossby waves. *Rev. Geophys. Space Phys.*, **17**, 1935–1949.

——, 1986: Seasonal variations of the 40–50-day oscillation in the tropics. *J. Atmos. Sci.*, **43**, 3138–3158.

——, and P. R. Julian, 1971: Detection of a 40–50-day oscillation in the zonal wind in the tropical Pacific. *J. Atmos. Sci.*, **28**, 702–708.

——, and ——, 1972: Description of global-scale circulation cells in the tropics with a 40–50-day period. *J. Atmos. Sci.*, **29**, 1109–1123.

Magana, V., and M. Yanai, 1991: Tropical–midlatitude interaction on the time scale of 30 to 60 days during the northern summer of 1979. *J. Climate*, **4**, 180–201.

Mahlman, J. D., and L. J. Umscheid, 1984: Dynamics of the middle atmosphere: Successes and problems of the GFDL "SKYHI" general circulation models. *Dynamics of the Middle Atmosphere*, J. R. Holton and T. Matsuno, Eds., Terra Scientific, 501–525.

Manabe, S., J. Smagorinsky, and R. F. Strickler, 1965: Simulated climatology of a general circulation model with a hydrologic cycle. *Mon. Wea. Rev.*, **93**, 769–798.

——, D. G. Hahn, and J. L. Holloway, Jr., 1979: Climate simulations with GFDL spectral models of the atmosphere: Effect of truncation. GARP Publ. Ser. No. 22, Vol. 1, 41–94.

Maruyama, T., 1982: Upper tropospheric zonal oscillation with a 30–50-day period over the equatorial western Pacific observed in cloud movement vectors. *J. Meteor. Soc. Japan*, **60**, 172–182.

Matsuno, T., 1966: Quasi-geostrophic motions in the equatorial area. *J. Meteor. Soc. Japan*, **44**, 25–43.

Miyahara, S., 1987: A simple model of the tropical intraseasonal oscillation. *J. Meteor. Soc. Japan*, **65**, 341–351.

Murakami, M., 1979: Large-scale aspects of deep convective activity over the GATE area. *Mon. Wea. Rev.*, **107**, 994–1013.

Murakami, T., 1987: Intraseasonal atmospheric teleconnection patterns during the Northern Hemisphere summer. *Mon. Wea. Rev.*, **115**, 2133–2154.

——, 1988: Intraseasonal atmospheric teleconnection patterns during the Northern Hemisphere winter. *J. Climate*, **1**, 117–131.

——, T. Nakazawa, and J. He, 1984: On the 40–50 day oscillations during the 1979 Northern Hemisphere summer. Part I: Phase propagation. *J. Meteor. Soc. Japan*, **62**, 440–468.

——, ——, and ——, 1984: On the 40–50 day oscillations during the 1979 Northern Hemisphere summer. Part II: Heat and moisture budget. *J. Meteor. Soc. Japan*, **62**, 469–484.

Nakazawa, T., 1986: Intraseasonal variations of OLR in the tropics during the FGGE year. *J. Meteor. Soc. Japan*, **64**, 17–34.

——, 1988: Tropical super clusters within intraseasonal variations over the western Pacific. *J. Meteor. Soc. Japan*, **66**, 823–839.

Neelin, J. D., I. M. Held, and K. H. Cook, 1987: Evaporation–wind feedback and low-frequency variability in the tropical atmosphere. *J. Atmos. Sci.*, **44**, 2341–2348.

Nishi, N., 1989: Observational study on the 30–60-day variations in the geopotential and temperature fields in the equatorial region. *J. Meteor. Soc. Japan*, **67**, 187–203.

Nogués-Paegle, J., B.-C. Lee, and V. E. Kousky, 1989: Observed modal characteristics of the intraseasonal oscillation. *J. Climate*, **2**, 496–507.

Numaguti, A., and Y.-Y. Hayashi, 1991a: Behavior of cumulus activity and the structures of circulations in an "aqua planet" model. Part I: The structure of the super clusters. *J. Meteor. Soc. Japan*, **69**, 541–561.

——, and ——, 1991b: Behavior of cumulus activity and the structures of circulations in an "aqua planet" model. Part II: Eastward-moving planetary scale structure and the intertropical convergence zone. *J. Meteor. Soc. Japan*, **69**, 563–579.

Park, C.-K., D. M. Straus, and K. M. Lau, 1990: An evaluation of the structure of tropical intraseasonal oscillations in three general circulation models. *J. Meteor. Soc. Japan*, **68**, 403–417.

Pitcher, E. J., and J. E. Geisler, 1987: The 40- to 50-day oscillation in a perpetual January simulation with a general circulation model. *J. Geophys. Res.*, **92**, 11 971–11 978.

Salby, M. L., and R. R. Garcia, 1987: Transient response to localized episodic heating in the tropics. Part I: Excitation and short-time near-field behavior. *J. Atmos. Sci.,* **44,** 458–498.

——, D. L. Hartmann, P. L. Bailey, and J. C. Gille, 1984: Evidence for equatorial Kelvin modes in *Nimbus-7* LIMS. *J. Atmos. Sci.,* **41,** 220–235.

Sheng, J., and Y. Hayashi, 1990: Observed and simulated energy cycles in the frequency domain. *J. Atmos. Sci.,* **47,** 1243–1254.

Sui, C.-H., and K.-M. Lau, 1989: Origin of low-frequency (intraseasonal) oscillations in the tropical atmosphere. Part II: Structure and propagation of mobile wave–CISK modes and their modification by lower boundary forcings. *J. Atmos. Sci.,* **46,** 37–56.

Swinbank, R. T., N. Palmer, and M. K. Davey, 1988: Numerical simulations of the Madden and Julian oscillations. *J. Atmos. Sci.,* **45,** 774–788.

Takahashi, M., 1987: A theory of the slow phase speed of the intraseasonal oscillation using the wave–CISK. *J. Meteor. Soc. Japan,* **65,** 43–49.

Tokioka, T., K. Yamazaki, A. Kitoh, and T. Ose, 1988: The equatorial 30–60-day oscillation and the Arakawa–Schubert penetrative cumulus parameterization. *J. Meteor. Soc. Japan,* **66,** 883–901.

Trenberth, K. E., 1984: Interannual variability of the Southern Hemisphere circulation: Representativeness of the year of the global weather experiment. *Mon. Wea. Rev.,* **112,** 108–123.

——, and J. G. Olson, 1988: An evaluation and intercomparison of global analyses from the National Meteorological Center and the European Centre for Medium-Range Weather Forecasts. *Bull. Amer. Meteor. Soc.,* **69,** 1047–1057.

Van Tuyl, A. H., 1987: Nonlinearities in low-frequency equatorial waves. *J. Atmos. Sci.,* **17,** 2478–2492.

Wallace, J. M., and V. E. Kousky, 1968: Observational evidence of Kelvin waves in the tropical stratosphere. *J. Atmos. Sci.,* **25,** 280–292.

Wang, B., 1988: Dynamics of the tropical low-frequency waves. An analysis of the moist Kelvin waves. *J. Atmos. Sci.,* **45,** 2051–2065.

——, and H. Rui, 1990: Dynamics of the coupled moist Kelvin–Rossby wave on an equatorial beta-plane. *J. Atmos. Sci.,* **47,** 397–413.

Webster, P. J., 1983: Mechanism of monsoon low frequency variability: Surface hydrological effects. *J. Atmos. Sci.,* **40,** 2110–2124.

——, and L. C. Chou, 1980: Low frequency transitions of a simple monsoon system. *J. Atmos. Sci.,* **37,** 368–382.

Xie, S.-P., 1991: Evaporation–wind feedback and the organizing of tropical convection on the planetary scale: A theory of tropical intraseasonal oscillations. Ph.D. thesis, Tohoku University, Sendai, Japan, 133 pp.

——, and A. Kubokawa, 1990: On the wave–CISK in the presence of a frictional boundary layer. *J. Meteor. Soc. Japan,* **68,** 651–657.

Yamagata, T., 1987: A simple moist model relevant to the origin of intraseasonal disturbances in the tropics. *J. Meteor. Soc. Japan,* **65,** 153–165.

——, and Y. Hayashi, 1984: A simple diagnostic model for the 30–50-day oscillation in the tropics. *J. Meteor. Soc. Japan,* **62,** 709–717.

Yanai, M., and T. Maruyama, 1966: Stratospheric wave disturbances propagating over the equatorial Pacific. *J. Meteor. Soc. Japan,* **44,** 291–294.

Yano, J.-I., and K. Emanuel, 1991: An improved model of the equatorial troposphere and its coupling with the stratosphere. *J. Atmos. Sci.,* **48,** 377–389.

Yasunari, T., 1981: Structure of an Indian summer monsoon system with around 40-day period. *J. Meteor. Soc. Japan,* **59,** 336–354.

Yoshizaki, M., 1991: Selective amplification of the eastward-propagating mode in a positive-only wave–CISK model on an equatorial beta plane. *J. Meteor. Soc. Japan,* **69,** 353–373.

Zebiak, S. E., 1989: On the 30–60-day oscillation and the prediction of El Niño. *J. Climate,* **2,** 1381–1387.

Zhao, J.-X., and M. Ghil, 1991: Nonlinear symmetric instability and intraseasonal oscillations in the tropical atmosphere. *J. Atmos. Sci.,* **48,** 2552–2568.